Interannual long equatorial waves in the tropical Atlantic from a high-resolution ocean general circulation model experiment in 1981-2000

Serena Illig, Boris Dewitte, Nadia Ayoub, Yves du Penhoat, Gilles Reverdin, Pierre de Mey, Fabrice Bonjean, Gary S.E. Lagerloef

Interannual long equatorial waves in the tropical Atlantic from a high-resolution ocean general circulation model experiment in 1981–2000

S. Illig,[1] B. Dewitte,[2] N. Ayoub,[1] Y. du Penhoat,[1] G. Reverdin,[3] P. De Mey,[1] F. Bonjean,[4] and G. S. E. Lagerloef[4]

Received 8 January 2003; revised 29 September 2003; accepted 29 October 2003; published 24 February 2004.

[1] We investigate the tropical Atlantic vertical structure variability (1981–2000) based on the CLIPPER ocean general circulation model (OGCM). We aim at determining to what extent the observed interannual variability can be explained by the low-frequency wave dynamics. The linear vertical modes of the OGCM climatological stratification are estimated along the equator. The baroclinic mode contributions to surface zonal current and sea level anomalies are calculated and analyzed at interannual timescales. The second baroclinic mode is the most energetic. The first (third) mode exhibits a variability peak in the west (east). The summed-up contribution of the high-order baroclinic modes (4–6) is as energetic as the gravest modes and is largest in the east. Wave components are then derived by projection onto the associated meridional structures. The effect of longitudinal boundaries near the equator is taken into consideration. Equatorial Kelvin and Rossby waves propagations, with phases speed close to the theory, are identified for the first three baroclinic modes. The comparison with a multimode linear simulation corroborates the propagating properties of the OGCM waves coefficients. An estimation of the meridional boundary reflection efficiency indicates that wave reflections take place at both boundaries. A 65% reflection efficiency is found at the eastern boundary. Our study suggests that low-frequency wave dynamics is to a large extent at work in the tropical Atlantic. On the basis of what is known on the Pacific El Niño-Southern Oscillation mode this may provide a guidance for investigating ocean-atmosphere mechanisms that can lead to the Atlantic zonal equatorial mode. *INDEX TERMS:* 4231 Oceanography: General: Equatorial oceanography; 4215 Oceanography: General: Climate and interannual variability (3309); 4255 Oceanography: General: Numerical modeling; *KEYWORDS:* tropical Atlantic interannual variability, long equatorial waves

Citation: Illig, S., B. Dewitte, N. Ayoub, Y. du Penhoat, G. Reverdin, P. De Mey, F. Bonjean, and G. S. E. Lagerloef (2004), Interannual long equatorial waves in the tropical Atlantic from a high-resolution ocean general circulation model experiment in 1981–2000, *J. Geophys. Res.*, *109*, C02022, doi:10.1029/2003JC001771.

1. Introduction

[2] The modes of variability that regulate the climate in the tropical Atlantic at interannual and decadal timescales are an interhemispheric SST mode often referred to as the Atlantic dipole [*Weare*, 1977; *Servain*, 1991; *Nobre and Shukla*, 1996; *Chang et al.*, 1997] and a zonal equatorial mode [*Merle et al.*, 1980; *Hisard*, 1980; *Philander*, 1986]. The dipole mode has received a great interest in recent years. Not only does it have no counterpart in the Pacific Ocean, but it is also suspected to be involved in the tropical-midlatitude connections [*Rajagopalan et al.*, 1998; *Tourre et al.*, 1999]. As for the so-called Atlantic El Niño mode, it is now clear that its dynamics is likely to share many characteristics with the Pacific El Niño-Southern Oscillation (ENSO) mode as suggested by *Zebiak* [1993], i.e., coupled instabilities whose characteristics strongly depend on the signature of the long equatorial waves on sea surface temperature (SST). From observations analysis, *Servain* [1991] and *Carton and Huang* [1994] suggest a relaxation of the trade winds in the western Atlantic that leads to an accumulation of warm water in the eastern Atlantic, similar to what happens in the Pacific during El Niño. *Wang* [2002] also shows that although not as strong, the positive ocean-atmosphere interaction associated with the Pacific Walker cell responsible for the Pacific El Niño, is also operating in the Atlantic. The analogy is however complicated by the fact that there may be a possible linkage between the Atlantic equatorial mode and the meridional gradient mode [*Servain et al.*, 1999, 2000; *Sutton et al.*, 2000] and that ENSO may act as a remote forcing of the equatorial Atlantic variability [*Zebiak*, 1993; *Delecluse et al.*, 1994; *Enfield*

[1] Laboratoire d'Etudes en Géophysique et Océanographie Spatiales, UM 5566 (CNES-CNRS-IRD-UPS), Toulouse, France.
[2] Institut de Recherche pour le Développement–Laboratoire d'Etudes en Géophysique et Océanographie Spatiales, Nouméa, New Caledonia.
[3] Laboratoire d'Océanographie Dynamique et de Climatologie, Paris, France.
[4] Earth and Space Research, Seattle, Washington, USA.

0148-0227/04/2003JC001771

and Mayer, 1997]. Long equatorial waves have been invoked to support processes responsible for some aspects of the interannual variability in the tropical Atlantic: *du Penhoat and Treguier* [1985] and *du Penhoat and Gouriou* [1987] have already shown that some aspects of the seasonal and interannual variability could be inferred from a linear model. However, there is still the difficulty to identify from observations a clear signature of equatorial waves in the equatorial Atlantic [*Arnault et al.*, 1990; *Handoh and Bigg*, 2000]. First, the small dimension of the basin, with respect to the expected speed of the waves, and the presence of longitudinal boundaries close to the equator in the Gulf of Guinea and near the Brazilian coasts, hinder the identification of a specific equatorial wave (it takes less than a month for a first-baroclinic mode Kelvin wave to cross the basin). It is also difficult to identify reflections of the waves at the coastlines, which are not straight. Note also the presence of a strong western boundary current, the North Brazil Current (NBC), which may also modify reflections of Rossby waves compared to what is predicted by linear theory. Second, with a shallower equatorial mean thermocline than in the Pacific, it is likely that a large number of baroclinic modes is required to represent the surface circulation. For instance, *du Penhoat and Treguier* [1985] have implemented 9 baroclinic modes in their linear model. The observed deep circulation in the tropical Atlantic indicates also a rich vertical structure [*Gouriou et al.*, 2001]. At last, the relatively large amplitude of the seasonal cycle (seasonal variability larger by an average factor of 1.5 than in the equatorial Pacific for SST when comparing the indices ATL3 (20°–0°W; 3°S–3°N) and NINO3 (150°–90°W; 5°S–5°N) from the Reynolds SST data in 1982–1998) as compared to the interannual variability (interannual variability weaker by an average factor of 2.44 than in the equatorial Pacific for SST) as already observed by *Picaut et al.* [1984], may render the use of the linear theory hazardous by coupling frequencies through nonlinear terms.

[3] The purpose of this paper is thus to determine to which extent linear theory can explain the interannual variability in the tropical Atlantic. This is somehow a prerequisite before interpreting the observations, the altimetric data being of particular interest. From a more general perspective, this is believed to constitute useful material for the interpretation of the zonal equatorial mode. In particular, can we really talk of an ''Atlantic El Niño''?, which would require, for instance, the existence of long equatorial wave reflections at the meridional boundaries. The approach proposed here consists in confronting the results of the projection of a high-resolution ocean general circulation model (OGCM) simulation on the equatorial normal modes to linear multimode model simulations. A similar approach was used by *Dewitte et al.* [1999, 2003] for the tropical Pacific and shown to be successful in depicting the low-frequency vertical structure variability. It is applied here for the first time in the tropical Atlantic with all the difficulties that arise from the specificities of this ocean mentioned above as compared to the tropical Pacific. Our results indicate that such methodology with some adjustments is able to bring new insights on the interannual variability and the mechanisms involving long equatorial waves in the tropical Atlantic.

[4] The paper is organized as follows. First, we describe the model and data used, followed by a brief comparison between the model mean structure and the interannual variability and observations during the 1981–2000 period. Then, a vertical mode decomposition of the OGCM is performed and the baroclinic mode contributions to pressure and current anomalies are studied. The long equatorial waves components are derived for each of the gravest baroclinic mode contributions and their propagating characteristics are analyzed. The results are then compared to equivalent ones of a multimode linear simulation using the projection coefficients and phase speed values derived from the OGCM simulation. Section 5 is devoted to the study of the reflection efficiency at the meridional boundaries. In particular, the influence of the longitudinal boundaries on the waves reflection is investigated in the Gulf of Guinea and near the Brazilian coasts. Our closing discussion summarizes these results and provides perspectives for this work.

2. CLIPPER Simulation

2.1. Basic Model's Characteristics

[5] We use the so-called CLIPPER ATL6 numerical simulation performed for the French CLIPPER project and kindly provided to us by the CLIPPER project team. We briefly review its main characteristics. For an exhaustive description the reader is invited to refer to the report of *Barnier and the CLIPPER Project Team* [2000].

[6] CLIPPER simulations are based on the primitive equations OPA model developed at the LODYC [*Madec et al.*, 1998]. The domain covers the whole Atlantic Ocean from 98.5°W to 0°E, 75°S to 70°N, with realistic coastlines and bathymetry and with 4 open boundaries (Drake, 30°E, 70°N, Gulf of Cadix) [*Tréguier et al.*, 2001]. The horizontal resolution is 1/6° on a Mercator isotropic grid. The meridional resolution varies from 4.8 km at the highest latitudes to 18.5 km at the equator. The vertical grid contains 43 levels, with 14 levels in the top 300 m. The motivations for using a model with such a high resolution are twofold. First, since our study focuses on the analysis of the vertical modes, we wish to have a reasonably high resolution on the vertical, which allows for a realistic representation of thermocline position and temperature gradients. Also, the meridional resolution should be good in the vicinity of the equator, considering that the energy projects onto the high-order baroclinic modes (see section 3) and that the associated equatorial waves have a fine meridional scale at the equator. Second, the high resolution allows for a more realistic simulation of the western boundary currents, in particular the NBC. Because of nonlinear interactions at these boundary current scales [*Arhan et al.*, 1998], the high resolution is likely to be important for the investigation of the Rossby waves reflections at the continental boundaries. For convenience, we started working with the OGCM fields averaged on a 1/3° × 1/3° grid (as an indication, the equatorial Rossby radius of the 6th baroclinic mode is of the order of 140 km (1.2°)). This was a posteriori checked as appropriate, considering the results of the vertical mode decomposition : most of the energy projects on the six first baroclinic modes. Note that we do not exclude from the analysis the baroclinic modes with a Rossby radius lower than 1/3°, since those are resolved by the model

with the 1/6° × 1/6° resolution. OGCM fields are monthly averaged before the analysis.

[7] After a 8-year spin-up forced by a monthly mean climatology of air-sea fluxes (see hereafter), the model has been integrated for 22 years, with daily forcing from ECWMF reanalysis ERA-15 fields from January 1979 to December 1993, and the operational analysis fields from January 1994 to December 2000. The forcing is the sum of the ECMWF net flux term and a relaxation term to observed SST [*Reynolds and Smith*, 1994]; the relaxation formulation is from *Barnier et al.* [1995]. Evaporation minus precipitation flux is used, but a relaxation to observed Sea Surface Salinity (SSS) from *Reynaud et al.* [1998] is added.

[8] Viscosity and vertical diffusivity are computed from a 1.5 turbulent closure model in which the evolution of the turbulent kinetic energy is given by a prognostic equation [*Blanke and Delecluse*, 1993].

[9] In the following, the OGCM simulation will be analyzed over the 20-year period extending from 1981 to 2000 and will be referred as CLIPPER.

2.2. CLIPPER Skills in the Tropical Atlantic

[10] In this section, we check the consistency between CLIPPER and observations in the tropical Atlantic. It is beyond the scope of this paper to present systematic and exhaustive model/data comparison. Instead, we focus on the quantities that control the equatorial waves characteristics, i.e., the mean structure along the equator, which controls the vertical mode structure (see section 3), and the interannual variability characteristics of surface zonal current and sea level, which also determine the baroclinic mode contributions. Note that the seasonal cycle of the CLIPPER simulation has already been analyzed by *Barnier and the CLIPPER Project Team* [2000]. The results indicates that CLIPPER has similar skills than the models used by the Community Modeling Effort (CME) in reproducing the observed seasonal variability (A. M. Treguier, personal communication).

2.2.1. Observations

2.2.1.1. EQUALANT Data

[11] The 1999 EQUALANT cruise (hereafter EQ99) took place in boreal summer 1999 (13 July to 21 August 1999). Meridional sections from 6°S to 6°N were conducted at 35°W, 23°W and 10°W (101 hydrologic stations). We compared the CLIPPER surface and subsurface zonal currents to the observed currents from a Shipboard Acoustic Doppler Current Profiler (S-ADCP, RDI BB 150 KHz, with a 4 m resolution). The reader is invited to refer to *Gouriou et al.* [2001].

2.2.1.2. Reynaud Atlas

[12] *Reynaud et al.* [1998] produced an annual climatology over the north and tropical Atlantic on a 1° × 1° spatial grid using approximately 90,000 conductivity-temperature-depth (CTD)-based temperature and salinity profiles from the National Oceanographic Data Center archives and from the World Ocean Circulation Experiment data.

2.2.1.3. TAOSTA

[13] *Vauclair and du Penhoat* [2001] have collected near surface and subsurface in situ temperature observations of the tropical Atlantic ocean between 1979 and 1998, and have built a surface and subsurface bimonthly temperature fields (Tropical Atlantic Ocean Subsurface Temperature Atlas: TAOSTA: http://medias.obs-mip.fr/taosta/). The interpolation is based on an objective analysis method [*Bretherton et al.*, 1976] and provides a gridded data set from 70°W to 12°E and from 30°S to 30°N on a 2° × 2° spatial grid with 14 vertical levels (same as those of *Levitus et al.* [1998]).

2.2.1.4. T/P+ERS Altimetric Data

[14] Sea level anomaly (SLA) maps supplied by AVISO (CLS, Toulouse, France) from 1993 to 2000 are used. The maps result from an optimal interpolation of combined altimetric data from TOPEX/POSEIDON and ERS1/2 missions [*Le Traon et al.*, 1998] on 1/4° × 1/4° grid every 10 days. The SLA is built by removing from the measurements the mean sea surface over 7 years (1993–1999). The accuracy of this product is of about 2–3 cm rms.

2.2.1.5. Zonal Currents Derived from Altimetry

[15] Surface currents (hereafter BL currents) are calculated from T/P altimeter data [*Lagerloef et al.*, 1999], wind vector data from SSM/I [*Atlas et al.*, 1996] and Reynolds SST. The diagnostic model [*Bonjean and Lagerloef*, 2002] is derived from quasi-steady and linear physics of the near-surface circulation and allows direct estimate of the 0–30 m layer velocity. The method was adjusted and validated in a study of the tropical Pacific circulation, and is here extended to the tropical Atlantic basin from October 1992 to December 2000.

2.2.2. Mean State

2.2.2.1. Temperature

[16] The mean structure (1981–1998) of CLIPPER temperature is compared to TAOSTA in the upper 250 meters (see Figure 1). In the surface layer, the simulation is cooler than the observations in the whole 10°S–10°N band; the difference is more important in the western part of the basin (>1°C). The largest differences are found within the thermocline, where the simulated temperature is on average warmer by 2°C, the thermocline is deeper (+18 m, identified as the depth of the 20°C isotherm), with weaker (−25%) vertical gradients than in the observations (identified as the thickness of the layer between the 16°C and 24°C isotherms). The meridional section at 23°W (see Figure 1b) shows differences between TAOSTA and CLIPPER in the thermocline, in particular in the region of the South Equatorial Under Current (SEUC) ∼[3°S; 100 m] and at the latitude of the North Equatorial Counter Current (NECC) ∼[8°N; 80 m], with differences larger than 3°C. These zonal currents are apparently in geostrophic balance since they are associated with the slope of the isotherms poleward and equatorward, respectively. The meridional gradients are weaker in the simulation than in the observations (∼−30%). The weaker slope of the isotherms in CLIPPER is associated with weaker currents and thus with weaker water mass transports (see paragraph devoted to the mean currents and Figure 2).

2.2.2.2. Salinity

[17] A comparison of the mean state (1981–2000) along the equator in the 250 first meters highlights differences between CLIPPER and the Reynaud atlas of the order of 0.2 psu. The largest discrepancies are found within the thermocline, in particular around (120 m; 38°W). There, the climatology exhibits large spatial gradients because of the salty waters of the North Brazil Under Current (NBUC), whose intensity is weak in CLIPPER (see next paragraph).

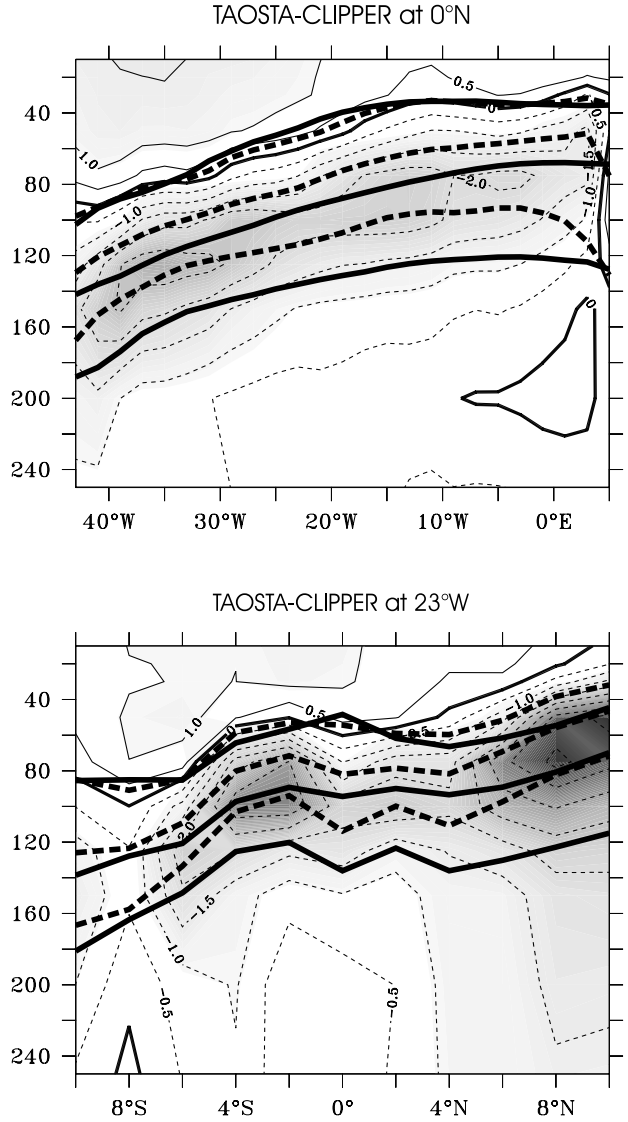

Figure 1. Longitude-depth section at the (top) equator and (bottom) latitude-depth section at 23°W of the difference between the mean in situ temperature (TAOSTA) and the mean CLIPPER temperature in the first 250 m over 1981–1998. The mean 16°C, 20°C, and 24°C isotherms are represented in plain thick lines for CLIPPER and in dashed thick lines for the observations. Unit is °C. Contour interval (CI) is 0.5°C. Values larger (lower) than 1°C (−1°C) are shaded.

Nevertheless, an inaccurate simulation of this field is not prejudicial to the results presented in this study, because the salinity variability has a weaker impact on the vertical structure of the gravest modes than the temperature variability (this was estimated with the results of a vertical mode calculation using climatological salinity).

2.2.2.3. Surface and Subsurface Currents

[18] In the absence of a comprehensive data set for investigating the mean current vertical structure, we present a qualitative comparison with the EQ99 data from the S-ADCP at 23°W for the month of July 1999 (see Figure 2). It has to be kept in mind that we use a monthly average of the CLIPPER outputs, whereas EQ99 is a snapshot. Consequently, the high-frequency component from the internal tides is present in EQ99 but not in the CLIPPER monthly average. The largest discrepancies between model and observations are for the magnitude of the main off-equatorial currents, which is partly due to the difference in time sampling. We find that the intensity and the position of the core of the Equatorial Under Current (EUC) in CLIPPER are in good agreement with EQ99 : the maximum of the EUC in CLIPPER (EQ99) is located around [0.3°N; 100 m] ([0.5°N; 84 m] [0.3°N; 100 m]) with a speed of 80 cm s^{-1} (90 cm s^{-1}). The locations of the transition zones between westward and eastward currents are in agreement with EQ99, so that the zonal and vertical scales of the main currents are correctly represented in

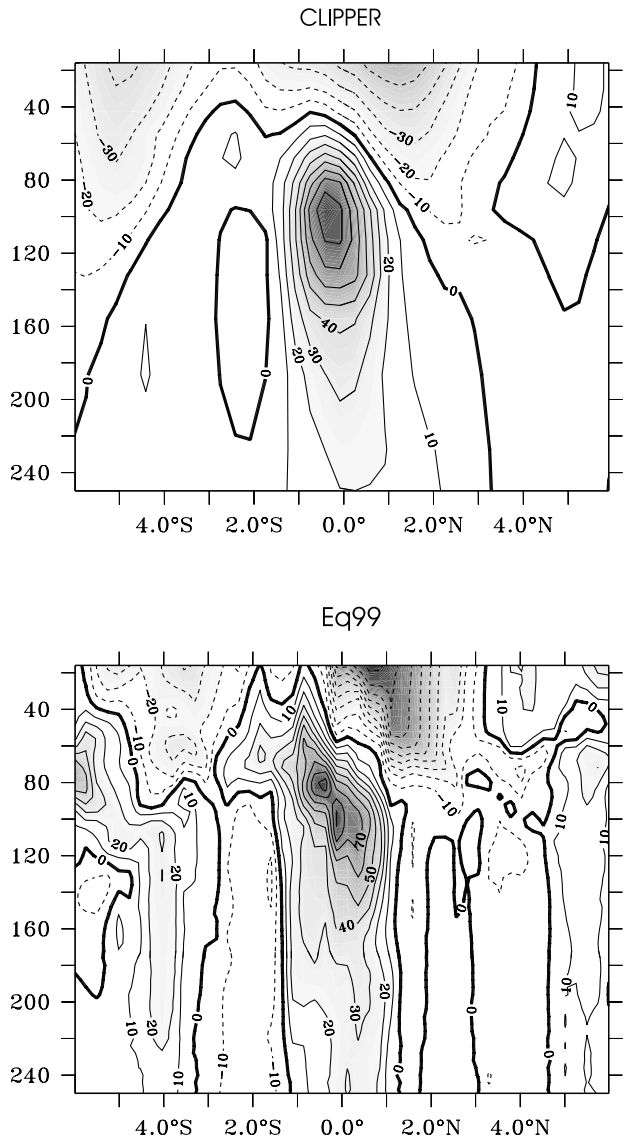

Figure 2. Latitude-depth section at 23°W in the first 250 m of the zonal current component (top) of the CLIPPER simulation in August 1999 and (bottom) for the 1999 EQUALANT cruise (EQ99) from 1 to 9 August 1999. Unit is cm s^{-1}. CI is 10 cm s^{-1}. Values larger (lower) than 20 cm s^{-1} (−20 cm s^{-1}) are shaded.

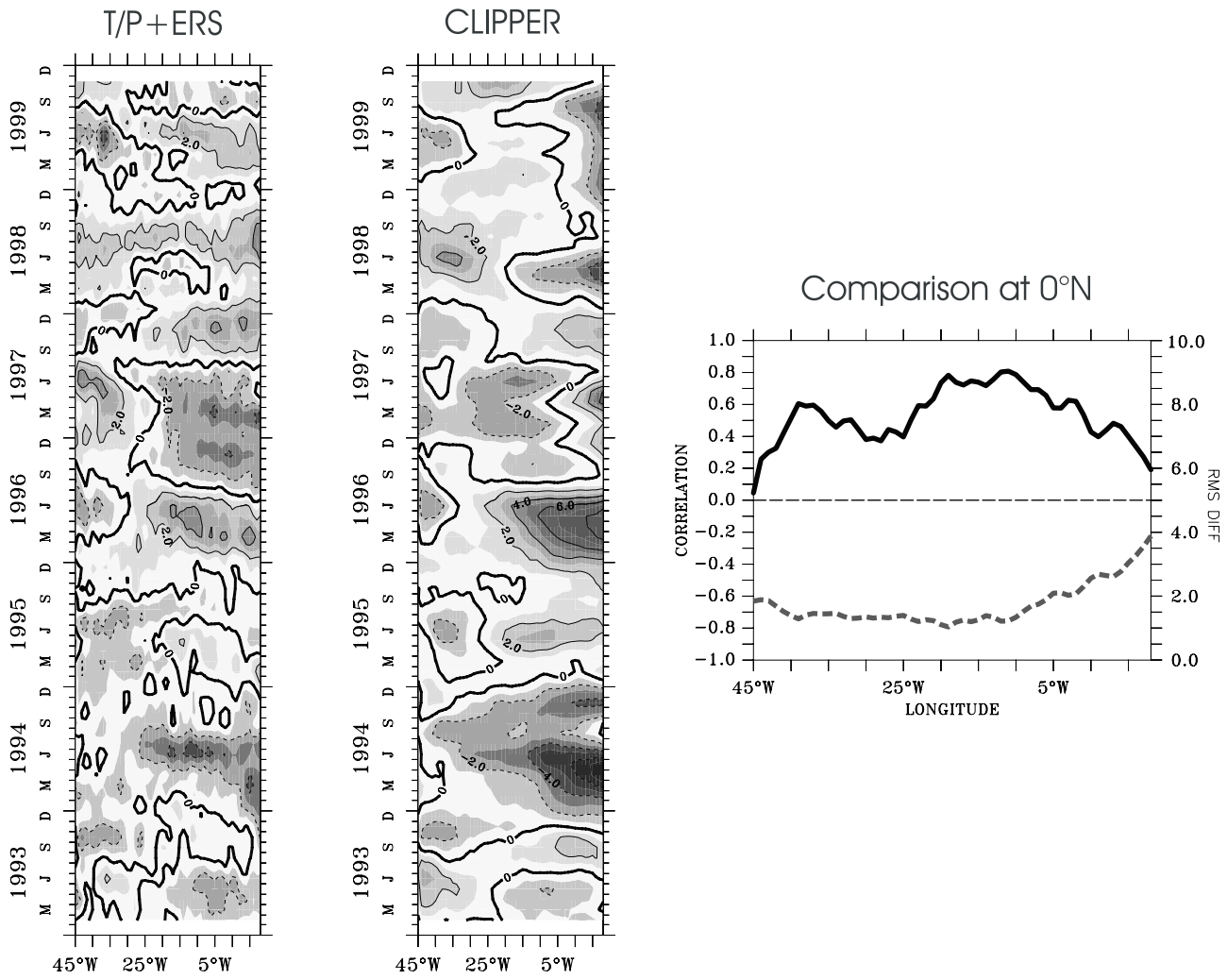

Figure 3. Longitude-time plot of T/P+ERS SLA and CLIPPER SLA along the equator over 1993–1999. Anomalies are relative to the seasonal cycle computed over 1993–1999. Unit is cm. CI is 2 cm. Positive values are red shaded, and negative values are blue shaded. (right) Plots of correlation (black thick line) and RMS difference (red dashed line) between CLIPPER and T/P+ERS for SLA are displayed. See color version of this figure at back of this issue.

CLIPPER, with clear identification of the equatorial branch of the South Equatorial Current (SEC) and the northern branch of the SEC, with a magnitude somewhat lower in the simulation. The signatures of the North Equatorial Under Current (South Equatorial Under Current) are suggested around (5°N, 80–90 m) (2°S, 120–200 m).

[19] The main features of the mean tropical Atlantic surface currents system and their seasonal variability are found to correspond to the ones estimated by *Richardson and McKee* [1984], *Arnault* [1987], and *Marin and Gouriou* [2000].

2.2.3. Interannual Variability

[20] Throughout the paper, interannual anomalies are defined relative to the seasonal cycle estimated over periods specific to each data set. For each intercomparison, the period considered for calculating the seasonal cycle and estimating the anomalies will be the common period between CLIPPER and the data set under consideration.

[21] A spectral analysis of the model thermocline depth anomalies (not shown) shows that a large part of the energy at interannual timescales is around 3–4 years, which corresponds to the sequence of interannual warm and cold events (see Figure 3). Some energy is also found in a peculiar 16-month peak, which is shared with other surface fields (currents, SST). It corresponds to an energy peak in the forcing fields.

2.2.3.1. Sea Level Anomalies

[22] The sea level from CLIPPER was computed with respect to the 1993–1999 mean field, using the "pressure compensation" approximation (see *Mellor and Wang* [1996] for the method). Simulated SLA interannual anomalies are compared to the combined altimetric data T/P+ERS (Figure 3). The longitude-time plots along the equator show that major features of the observed interannual variability of SLA are simulated by CLIPPER. CLIPPER and T/P+ERS SLA exhibits a coherent timing sequence of warm (1996 and 1998) and cold (1994 and 1997) events. Nevertheless, in the eastern basin the simulation presents a larger interannual variability compared to the observations, which makes the amplitudes of the interannual events larger and

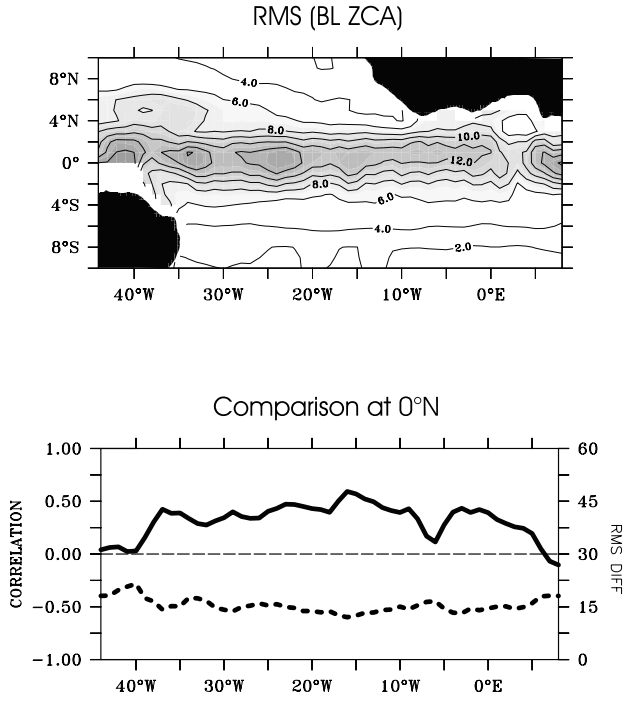

Figure 4. (top) Map of variability (RMS) of altimetric surface ZCA (BL ZCA) over 1993–1999. Anomalies are relative to the seasonal cycle computed over 1993–1999. Unit is cm s^{-1}. CI is 2 cm s^{-1}. Values larger than 6 cm s^{-1} are shaded. (bottom) Plots of correlation (plain line) and RMS difference (dotted line) between CLIPPER and BL for ZCA are displayed.

leads to larger RMS differences between CLIPPER and observed SLA. The correlation between model and observations is of the order of 0.6 in the central tropical Atlantic (correlation larger than 0.45 is significant at a 95% level of confidence [*Sciremammano*, 1979]). However, correlation decreases to values close to 0.1 near the continents. The RMS difference is less than 2 cm in the 4°S–4°N band, and remains in the error bar of the altimetric data (2–3 cm RMS). Along Brazil, north of the equator (around (46°W, 6°N)), where the retroflection takes place, the altimetric data maps display small-scale features, which are not simulated by the OGCM. This is a zone of large wind stress and heat fluxes variability as well.

2.2.3.2. Surface Current Anomalies

[23] Comparisons between CLIPPER and BL ZCA over 1993–1999 (Figure 4) indicate that there is a correct agreement between BL current anomalies and simulated ZCA. Variations along the equator of the CLIPPER ZCA and satellite-derived velocity are qualitatively similar, both indicating sporadic short events of a few month duration (3–5 months) with reversing large-scale anomalous currents over more than 20° and more. Patterns of correlation are consistent with those found in the SLA comparison, with highest correlations in the ATL3 region, and in the east just north of the equator (0.4 on average, correlation >0.28 remains at a 95% level of confidence [*Sciremammano*, 1979]). The RMS of the satellite-derived current anomalies is smaller, suggesting that either the amplitude of the CLIPPER ZCA is too large, or the variability of the satellite-derived current anomalies is too weak because of smoothed altimetry data for example (compare Figure 4 to Figure 5a; note, however, that the anomalies and the RMS are not calculated over the same period).

2.3. Atmospheric Forcing

[24] The results of the simulation are highly dependent on the wind forcing fields, especially in the tropics. These fields contain large errors that are very difficult to quantify precisely. A qualitative indication can be obtained by comparing the ECMWF products with observations on the 1993–1999 period: the monthly wind stress fields from ERS scatterometer provided by CERSAT [*Bentamy et al.*, 1996] and monthly pseudo wind stress fields from FSU (using $c_d = 1.6$) derived from in situ measurements [*Servain et al.*, 1997].

[25] Zonal anomalies have slightly larger amplitudes in the ECMWF product than in both observed data sets. They are positively correlated (correlation ~0.5 significant at a 95% level of confidence [*Sciremammano*, 1979]), except in the eastern part of the basin and in the Inter Tropical Convergence Zone (ITCZ), where the correlation is no longer significant and the variability is weak. In the eastern part of the basin, the wind variability (RMS) has different characteristics in the three wind products. In particular, the ECMWF winds exhibit a larger variability (with an average factor of 1.5 over ATL3) in the Gulf of Guinea compared to the ERS wind stress anomalies. The ECMWF wind meridional component has a larger variability than the ERS product in the eastern part of the basin and around (35°W; 6°N). The same comparison is done with the FSU winds. It exhibits slightly weaker correlations and similar zones of discrepancies (not shown), in particular in the eastern part of the basin, where the variability is larger in the ECMWF products (with a average factor of 1.3 over ATL3). This is a possible source of differences between the simulated and observed SLA in this area (Figure 3). We provide an estimate of the error in simulated SLA and Zonal Current Anomalies (ZCA) induced by wind biases in section 4 (see Table 2). Differences in RMS differences between model and observations for SLA in the ATL3@eq region (20°–0°W; 0°N) can reach 0.23 cm between FSU and ERS runs. It is worth pointing out that twin numerical experiments using respectively reanalyzed ECMWF fluxes and ERS momentum flux in the CLIPPER model (1/3° resolution) suggest that the ERS wind stress fields are more realistic than the ECMWF fields (Y. Quilfen, personal communication, 2001).

[26] A main question in any model-based study is to which extent the results can be generalized beyond the specific model set up, and how they apply to the real world. The brief comparison between observations and CLIPPER simulation presented above indicates that CLIPPER reproduces a large part of the mean structure. Although the reported biases have the ability to impact the baroclinic mode contributions (for example, through nonlinearities associated with the interaction between the background currents and the long equatorial waves), it is beyond the scope of the present paper to address such issues. What is very encouraging is that, major features of the observed interannual variability are captured by the OGCM. We will therefore investigate further in this simulation the baroclinic

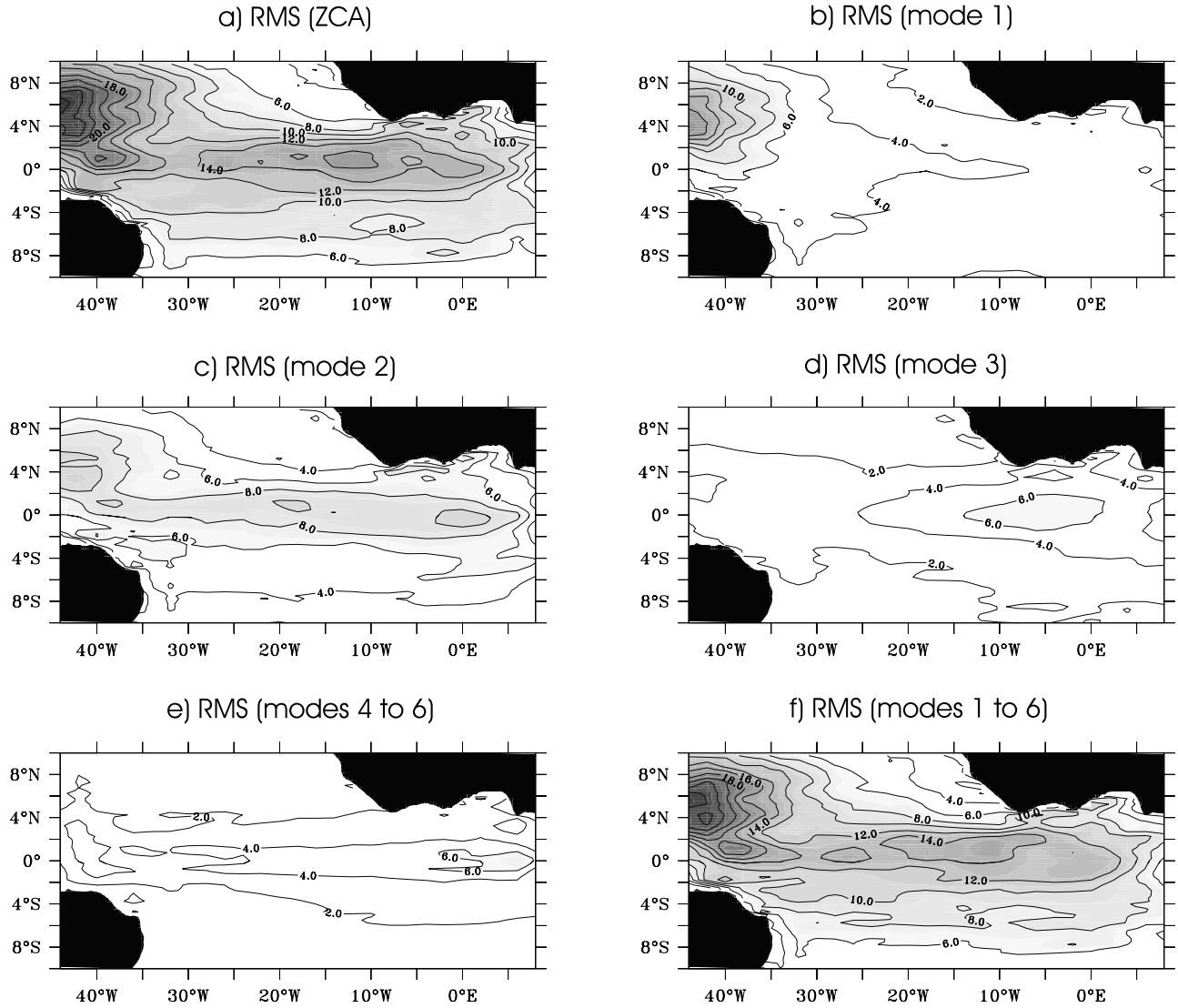

Figure 5. Map of variability (RMS) of (a) CLIPPER total surface ZCA over 1981–2000 and the contribution (b) of the first baroclinic mode, (c) of the second baroclinic mode, (d) of the third baroclinic mode, (e) of the sum of modes 4–6, and (f) the sum of the six gravest baroclinic modes of CLIPPER. Anomalies are relative to the seasonal cycle computed over 1981–2000. Unit is cm s^{-1}. CI is 2 cm s^{-1}. Values larger than 6 cm s^{-1} are shaded.

mode variability and their associated long equatorial waves contribution.

3. Long Equatorial Wave Variability

[27] In order to study the propagation of long equatorial waves, a vertical mode decomposition (as by *Dewitte et al.* [1999]) of the high-resolution CLIPPER simulation is first performed and then the long equatorial wave signal is extracted.

3.1. Vertical Mode Decomposition

[28] In order to take into consideration the zonally sloping thermocline, when carrying the vertical mode decomposition of the model variables, the decomposition is sought along the equator keeping the longitudinal dependence of the vertical functions F_n [*Dewitte et al.*, 1999]. Moreover, we also retained the seasonal dependence (labeled as t_{12}) of the vertical structure, as is has a relatively large amplitude [cf. *du Penhoat and Treguier*, 1985; *Picaut et al.*, 1984], and induces significant changes in the baroclinic mode contribution. (see Appendix A). Although linear theory usually assumes a steady background state, this is not believed to be prejudicial for the interpretation of the waves, considering the relative small time taken by the waves to travel back and forth across the basin, compared to seasonal variations of the stratification.

[29] The vertical structure functions $F_n(x, z, t_{12})$ are determined using the method described by *Dewitte et al.* [1999]. The potential density $\rho(x, y = 0, z, t_{12})$ is computed using the state equation from *Millero and Poisson* [1981] and an approximate Brunt-Vaïsälä frequency $N(x, y = 0°N, z, t_{12})$ is deduced. The vertical differential equation for the vertical modes n $((F_n)_z/N^2)_z + F_n/c_n^2 = 0$ [*Philander*, 1978] is

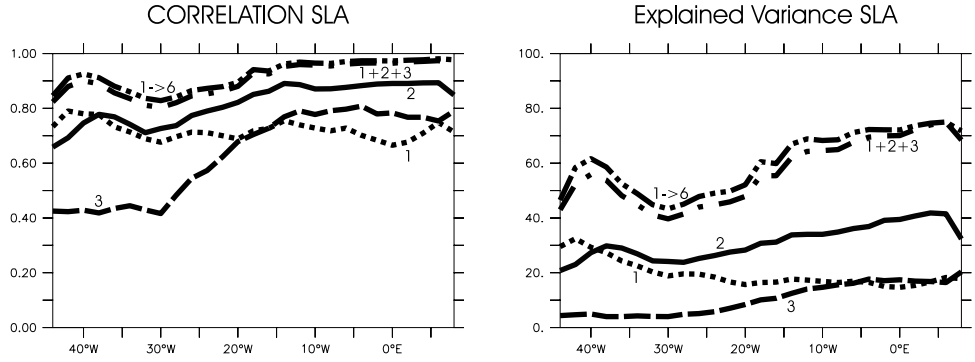

Figure 6. Plot of correlation and explained variance along the equator referenced to the total SLA for SLA mode 1 contribution (dotted line), mode 2 contribution (plain line), mode 3 contribution (dashed line), the sum of the first three modes (dot-dashed line), and the sum of the first six modes (doubled dot-dashed line). Anomalies are relative to the seasonal cycle computed over 1981–2000.

solved using a method based on an SVD decomposition. Zonal currents and pressure are then projected on the vertical structure functions: $q_n = \langle q(x, y, z, t) \times F_n(x, z, t_{12}) \rangle = \int_{H(x)}^{0} q(x, y, z, t) F_n(x, z, t_{12}) dz$, with q being u or p, and $H(x)$ the ocean depth.

[30] We first analyze the characteristics of the baroclinic modes variability. Theoretical Kelvin and Rossby mode contributions are then derived for the most energetic baroclinic modes. Their propagation characteristics are investigated in the light of what is expected from linear theory.

3.1.1. Zonal Current Anomaly Baroclinic Contribution

[31] The total ZCA are estimated by averaging the currents over the 3 uppermost levels of the model (5–30 m depth), in order to remove the shear within the weakly stratified surface layer associated with incomplete mixing which cannot be represented in the vertical mode decomposition.

[32] The RMS variability of the surface ZCA is presented in Figure 5a. Large values (>12 cm s^{-1}) are confined within 3°S–4°N, with maximum variability centered around (12°W, 1°N). The zone of maximum variability, north of 4°N and around 40°–45°W, corresponds to the retroflexion area of the North Brazil Current (NBC), where the dynamics is highly nonlinear and the wind stress curl variability is large. Therefore we do not expect to explain this variability only in terms of long equatorial waves. Note that this variability projects largely on the first and the second baroclinic modes, consistently with the large vertical scales associated with these currents [*Arhan et al.*, 1998]. Figures 5b and 5c display the contribution of the two gravest modes to the surface ZCA. For mode 1, the simulated variability is lower than 5 cm s^{-1} in most of the basin, with a peak of 15 cm s^{-1} in the western Atlantic at 4°N, whereas mode 2 is characterized by a larger variability (>8 cm s^{-1}) that is more confined toward the equator and that reaches a maximum amplitude (9–10 cm s^{-1}) in the center of the basin. Variability is also large around (45°W, 4°N). The contribution of the third baroclinic mode (Figure 5d) is confined to the 3°S–3°N band with a variability peak in the eastern part of the basin (>6 cm s^{-1}). Along the equator, the summed-up contribution of the three gravest modes explain from 30 to 60% of CLIPPER total surface current variability (RMS) from east to west (correlation coefficient c = 0.8 to 0.9) (not shown). The higher-order baroclinic (4–6) modes present a zone of large variability (>5 cm s^{-1}) located in the eastern part of the basin (around 5°W) along the equator (Figure 5e). This is due to the shallow thermocline, which induces a larger contribution of the high-order baroclinic modes. The variability of the summed-up contribution of modes 1 to 6 is shown in Figure 5f and explains 60% of the total variability (c = 0.9 on average along the equator).

3.1.2. Sea Level Anomaly Baroclinic Contribution

[33] As found for ZCA, the analysis of the individual contribution of each baroclinic mode reveals that the most energetic mode is the second mode which explains 20 to 35% of the total variability from west to east (c = 0.6 to 0.9) along the equator (see Figure 6). Mode 1 variability peaks in the west, whereas, the high-order baroclinic modes (4–6) variability is confined in the eastern part of the basin. The summed-up contribution of the first three baroclinic modes captures the basin wide pattern of the simulated SLA, with an associated explained variance of the order of 50% in the center part of the basin, reaching up to 70% in east. It is however only 40% around 30°W, indicating that a larger number of baroclinic modes is required to recover the SLA variability there. Note that this is an area where in the seasonal cycle there is a change in sign of the thermocline displacements from west to east (i.e., the mean pivot position of the thermocline) and where interannual anomalies are small (see Figure 3). This is the main difference between SLA and ZCA reconstruction from modes 1 to 3. Note also that, as for ZCA, the variability associated with the NBC retroflexion projects mostly on the first two gravest baroclinic modes (not shown).

3.2. Horizontal Mode Decomposition

3.2.1. Decomposition Method

[34] In this section, we study the meridional structure of the baroclinic modes. To do so, we project both the baroclinic contributions to ZCA and SLA from CLIPPER onto the complete basis of the long-wavelength meridional modes. These modes are computed from the zonally and seasonally varying phase speed obtained from the former vertical mode decomposition. The method takes explicitly into consideration the coasts close to the equator in the Gulf of Guinea and near South America, as by *Cane and Sarachik* [1979] (hereinafter referred to as CS79), so that

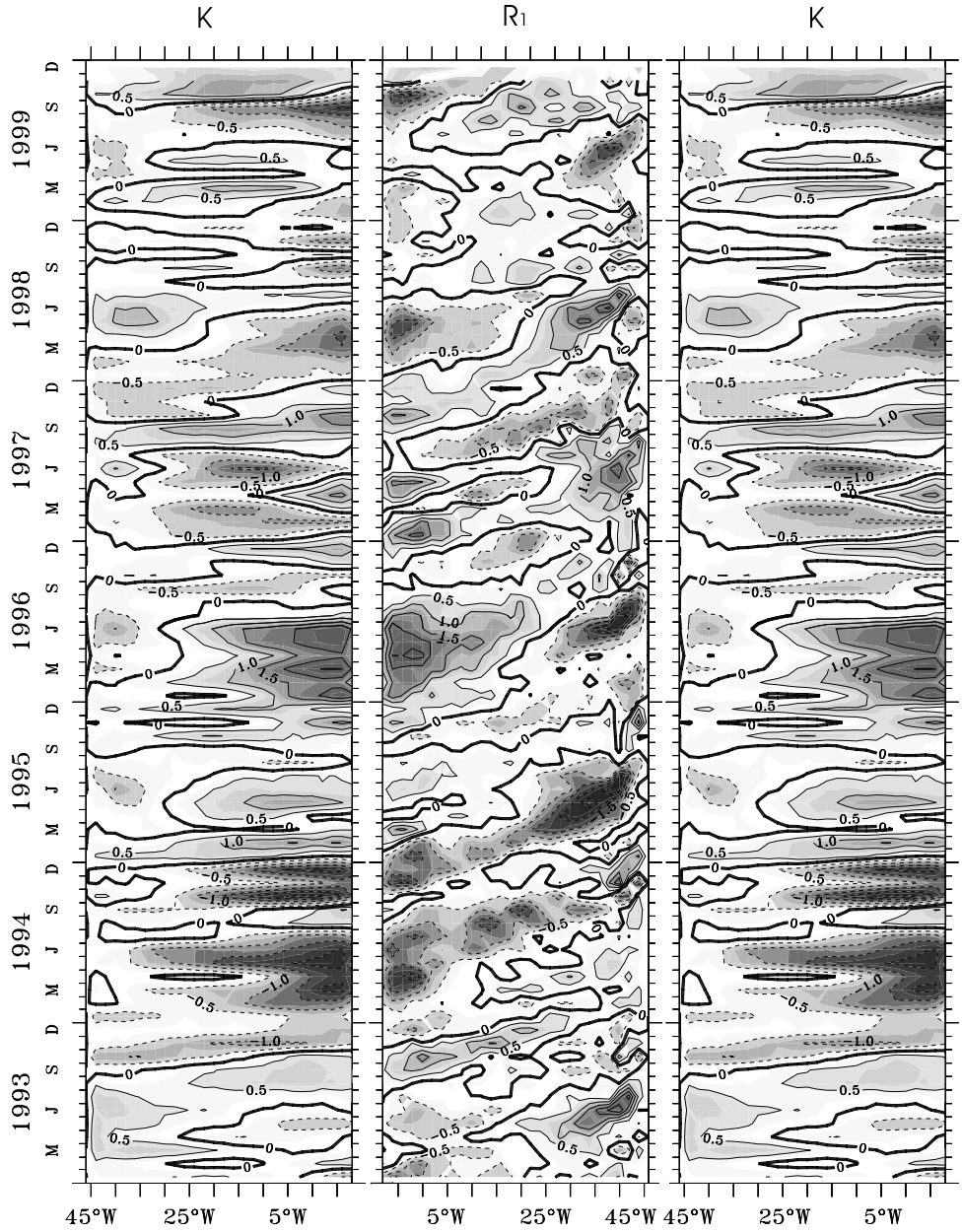

Figure 7. Longitude-time plot of the Kelvin (K at 0°N) and the first meridional Rossby at (R_1 at 3°N) component for the second baroclinic mode SLA over 1993–1999. Anomalies are relative to the seasonal cycle computed over 1993–1999. R_1 is displayed in reverse from 46°W to 8°E, and K is repeated in order to visualize reflections at the zonal boundaries. Unit is cm. CI is 0.5 cm. Positive values are red shaded, and negative values are blue shaded. See color version of this figure at back of this issue.

meridional modes are also a function of longitude. Further explanations are provided in Appendix B, which summarizes the formalism of CS79. The notations are those of CS79.

[35] In our computation, the projection is done over the 10°S–10°N band. Nevertheless, in agreement with the theory, anti-Kelvin waves (K^+) and Rossby-Kelvin waves (R_0) are not taken into consideration, because, over the whole basin, their structures have an infinite meridional extension in one direction at least (infinite extension south of the Gulf of Guinea and infinite extension north of the Brazilian coasts) (see CS79 for theoretical formulation).

[36] For the gravest vertical modes, the Kelvin and first meridional Rossby waves contribute to a large share of the equatorial variability in ZCA and SLA. For example, in the ATL3 region along the equator, the summed-up contribution of the Kelvin (hereafter K) and the first meridional Rossby (hereafter R_1) waves to SLA (ZCA) variability explains 66% (28%,), 79% (45%) and 63% (47%) for the baroclinic modes 1, 2 and 3 from the CLIPPER decomposition. So, we will focus on the analysis of the K and R_1 components.

3.2.2. Results of the Decomposition

[37] Figure 7 shows a time-longitude plot of K and R_1 contribution to SLA for the second baroclinic mode.

Table 1. Time-Averaged Phase Speed Values of Kelvin (K) and First Rossby (R_1) Waves for the Three First Baroclinic Modes (BM) in the Western and Eastern Basins[a]

	K		R_1	
	West	East	West	East
BM 1	2.94 (2.43)	2.66 (2.47)	0.79 (0.81)	0.78 (0.71)
BM 2	1.50 (1.48)	1.27 (1.33)	0.42 (0.49)	0.43 (0.43)
BM 3	1.00 (0.89)	0.89 (0.89)	0.29 (0.295)	0.29 (0.296)

[a]Theoretical values in parentheses are estimated from the results of the vertical decomposition from CLIPPER. Unit is m s^{-1}.

According to the location of the maximum in the sea level meridional waves structures (Figure B1), the K contribution is displayed along the equator and the R_1 contribution is presented at 3°N. The R_1 contribution is displayed in reverse and the K contribution is repeated to illustrate wave reflections at the African and South American coasts. This plot is suggestive of long wave propagations, since the wave patterns are consistent across the basin. A visual estimation of the times of propagations suggests phase speeds in agreement with the theoretical values (see Table 1 and section 3.2.3 for precise calculation). Moreover, the coherency of the K and R_1 components near the African coasts suggests that wave reflection takes place. This is less clear at the western boundary, although, the correlation between K and R_1 reaches 0.98 at 46°W, but drops further east. We defer further the interpretation of these plots to section 5, as it requests to separate the contribution of local wind forcing (as opposed to the remote forcing).

3.2.3. Propagation Characteristics

[38] Low-frequency linear waves have horizontal propagating phase speeds proportional to the separation velocity c_n. The propagation characteristics are estimated from a lag correlation analysis of the Kelvin (K) and the first Rossby (R_1) components for different longitudes.

[39] Figure 8 shows the results of the lag correlation analysis for the R_1 component of the three gravest baroclinic modes, with a reference longitude at 30°W (left panel) and 2°W (right panel). Shading indicates positive correlation with a level of significance larger than 95% [*Sciremammano*, 1979]. The slope of the least squares best fit to the points with maximum correlation at each longitude provides an estimation of the phase speed of the waves. The results are presented in Table 1. The theoretical time-averaged speed for the nth baroclinic K (R_1), which is reported in Table 1, is $c_n(c_n/(2\mu_n + 1))$, where c_n is derived from the vertical mode decomposition of the CLIPPER stratification and μ_n is the eigenvalue in the horizontal mode decomposition (cf. CS79). This indicates that the estimated phase speed values are in good agreement with the theoretical values: differences do not exceed 20%.

[40] The plots of Figure 8 exhibit a clear low-frequency first meridional Rossby wave signal with high coherency ($c > 0.5$) extended longitudinally over the whole basin. The secondary maximum for large lags ($|lag| > 80$ days) corresponds to the resonant basin mode K + R_1 (T = 117, 203, 305 days for the three first baroclinic modes respectively). The multiple wave reflections induce negative correlation patches.

[41] For the reference at 2°W, the zone of maximum correlation illustrates the westward propagation of R_1 waves from the eastern boundary. The pattern associated with positive correlations, with a level of significance larger than 95%, is broad in time, indicating a low-frequency forcing. The zonal extension of the "beams" to the west is consistent with propagation of free Rossby waves. The westward reduction of the beam width indicates energy dissipation processes. The plots with a reference longitude at 30°W are a mirror view of the above; that is, free propagating Rossby waves originate from the eastern basin and enter the forcing region (near 30°W).

[42] These results are highly suggestive of interannual equatorial wave propagation taking place in the OGCM. In order to check for the coherency with linear theory and estimate the impact of nonlinearities and diffusion processes on this variability, a comparison with a linear simulation is performed below.

4. Comparison With Linear Simulation

[43] The OGCM includes nonlinear terms and diffusive processes which couple horizontal and vertical equation. A simple multimode linear model will allow us to investigate if the projection of the CLIPPER fields on individual vertical modes behaves dynamically in a way similar to what is expected from the linear theory, (i.e., with wave dynamics characterized by the phase speed and the projection coefficients estimated from CLIPPER simulation).

4.1. Linear Model Description

[44] The linear model is the one used by *Cane and Patton* [1984], an adiabatic shallow-water model on a β plane. In the light of the OGCM baroclinic mode decomposition, the 6 gravest baroclinic modes are retained. For each baroclinic mode, the model first solves the equatorial Kelvin mode propagating eastward and then derives the long low-frequency Rossby and anti-Kelvin modes propagating westward. The model time step is 2 days. The basin configuration is almost similar to the one used by *du Penhoat and Treguier* [1985], from 28.875°S to 28.875°N with an horizontal resolution of 2° × 0.25°. To represent better the South American coast line, two steps are introduced, as suggested by the study of *du Penhoat et al.* [1983]: the first from 50°W to 44°W at 1.125°S and the second from 44°W to 36°W at 3.375°S.

[45] The wind stress is projected on the different vertical modes in term of a coefficient $P_n(x, t_{12})$, which we derive from the vertical mode decomposition. The wind stress is assumed to act like a body force in a mixed layer of thickness d, as:

$$P_n(x,t_{12}) = \frac{\frac{H_1}{d(x,t_{12})}\int_{-d(x,t_{12})}^{0} F_n(x,z,t_{12}).\,dz}{\int_{-H(x)}^{0} F_n^2(x,z,t_{12}).\,dz}$$

[46] H_1 is the adimensionalizing depth, equal to 150 m, and $d(x, t_{12})$ is the depth of the near-surface layer of weak stratification estimated from CLIPPER as the depth, along the equator, where the temperature is lower than the surface temperature by 1°C.

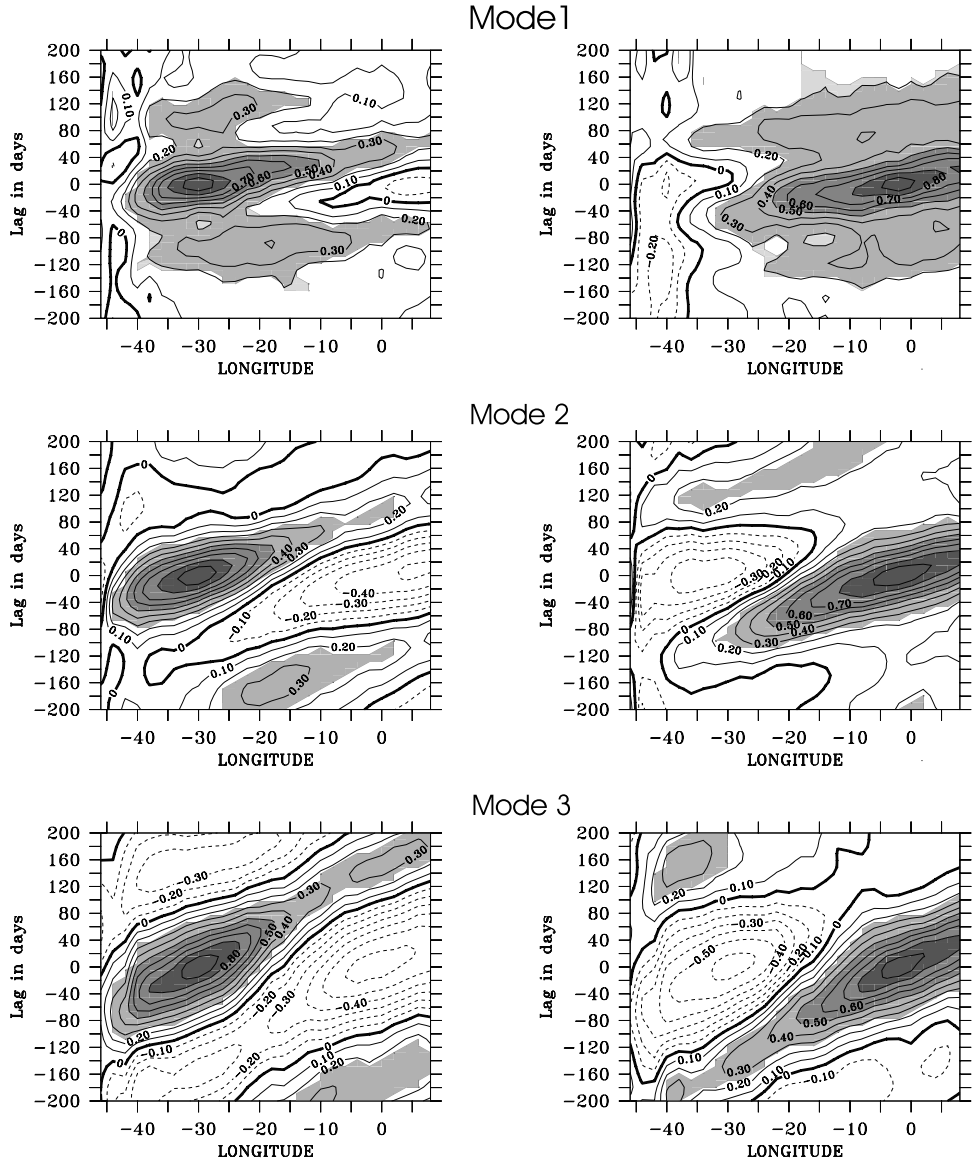

Figure 8. Lag correlation plots of the R_1 coefficient for the first three baroclinic modes of CLIPPER with a reference longitude at (left) 30°W and (right) 2°W. Lag is in days. Negative lag accounts for a delay with respect to instantaneous signal at the reference longitude. Shading denotes regions where correlation is significant at the 95% level.

[47] Figure 9 displays the time averaged values of $\overline{P_n(x,t_{12})}$ along the equator for the first six baroclinic modes. Not surprisingly, the wind stress coefficients of modes 2 and 3 are larger than for the other modes. Their magnitude increases from west to east consistently with the eastward shoaling of the thermocline. For high-order modes (4–6), P_n reaches similar values as for mode 1 near the Gulf of Guinea, consistently with the results of the baroclinic modes contributions to ZCA and SLA (Figures 5–6). P_n exhibits a noticeable seasonal variability, which is described in Appendix A.

[48] The model is forced by wind stress anomalies computed relative to the seasonal cycle over the period 1992–1999, following a spin-up with the year 1992 repeated five times. We test three different wind products: ECMWF, ERS and FSU (see section 2.3). Time-averaged phase speed values are chosen for a profile at 14°W, which is just east of the wave forcing region (see Figure 7): 2.39 m s^{-1}, 1.34 m s^{-1}, 0.88 m s^{-1}, 0.63 m s^{-1}, 0.48 m s^{-1}, and 0.42 m s^{-1} for mode 1, 2, 3, 4, 5 and 6 respectively. The comparison between altimetric observations (TP+ERS SLA and BL ZCA) and the three different runs indicates that the linear model exhibits good skills in reproducing the observed interannual variability and that these skills are comparable to CLIPPER performances (see section 3), whatever the wind products. Differences between ECMWF run and ERS and FSU runs in RMS difference between observations and linear model runs for SLA (ZCA) are lower than 11% (14%) of the ECMWF run variability (RMS) in ATL3 (cf. Table 2). The correlation exhibits differences lower than 0.09 (0.05) for SLA (ZCA). This suggests that the main characteristics of the CLIPPER

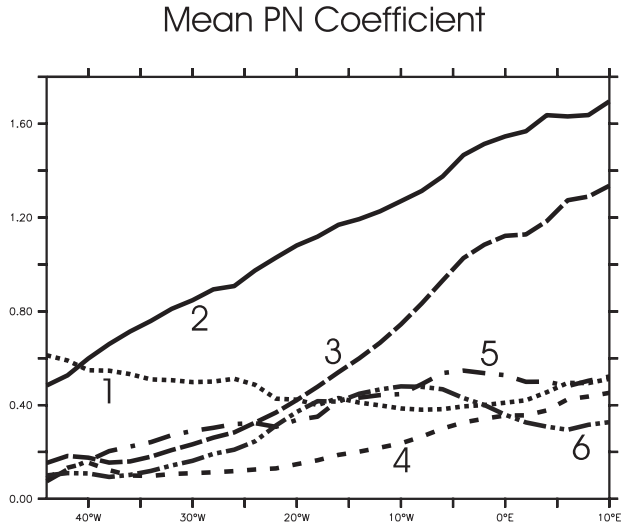

Figure 9. Mean wind projection coefficient of the linear model as a function of longitude for the first six baroclinic modes.

decomposition that have been evidenced in this study (see section 4) should hold with other winds than ECMWF. In the following, for the comparison between CLIPPER and the linear model, we will focus on the ECMWF forced linear model run.

[49] In the linear model, dissipation is modeled as a Rayleigh friction. Several tests were performed to choose the appropriate time decay for it. The same rule as by *Gent et al.* [1983] is used; that is, $r_n = r_1(c_n/c_1)^q$ with $q = 1.675$. This value for q is justified a posteriori in the light of the results of the CLIPPER horizontal mode decomposition (see section 5.1.2).

4.2. Baroclinic Mode Contribution

[50] Figure 10 displays the correlation and RMS differences between the linear simulation and the CLIPPER baroclinic decomposition, for individual baroclinic mode contributions to SLA and for the total SLA field as a function of longitude along the equator. A comparison with the altimetric data is also shown in the last panel. For the first baroclinic mode, correlation between CLIPPER and the wind driven equatorial wave model is of the order of 0.6, with an RMS difference lower than 0.8 cm. The linear model modes 2 and 3 also present a good agreement with CLIPPER with, however, a minimum of correlation around 20°–25°W, where the mean location of the pivot in the thermocline displacements is located (i.e., where the east-west seesaw takes places). The summed-up contribution of the six first baroclinic modes from the linear model is in good agreement with the SLA from CLIPPER with correlations larger than 0.6 to 0.7 from west to east and RMS difference lower than 2 cm on average. The level of agreement between the linear model SLA and T/P+ERS SLA is comparable to the one resulting from the comparison between CLIPPER SLA and T/P+ERS SLA (see Figure 3).

[51] Figure 11 presents variability maps of ZCA from the linear simulation, which should be compared to the CLIPPER decomposition displayed in Figure 5. Total surface current anomalies (Figure 11a) are derived from the contribution of the six first baroclinic modes added to Ekman current anomalies estimated as in *Blumenthal and Cane* [1989] (Climatological mixed layer depth was used and estimated from CLIPPER). Not surprisingly, the variability in the western part of the basin around 4°N is not reproduced by the linear simulation suggesting that this variability is associated to nonlinear processes. The contribution of mode 1 in the linear model is slightly weaker than for CLIPPER (−20% on average), with, however, a similar spatial structure, whereas mode 2 exhibits a slightly greater variability shifted to the west by 6°, with respect to CLIPPER. Mode 3 presents a variability with similar amplitude, but its maximum of variability is also shifted westward by about 8°–10°. The variability of the summed-up contribution of the six gravest baroclinic modes (Figure 11f) is larger than in CLIPPER, in particular around 15°W (+35%). The spatial structure is well reproduced by the linear model, but more confined toward the equator. Equatorial sections of correlation and RMS differences between the linear model and CLIPPER for total ZCA indicate correlation larger than 0.4 and RMS difference lower than 20 cm s^{-1} in the center of the basin (as illustrated by Table 2) and lower correlation near the meridional boundaries.

4.3. Propagation Characteristics

[52] A lag correlation analysis similar to the one in section 3.2 was performed on the wave coefficients for the linear model. Results are displayed on Figure 12 (to be compared to Figure 8). Results indicate that the patterns are in good agreement with CLIPPER for Kelvin (not shown) and Rossby wave coefficients in the western and eastern basins. The similar extension and slope of the "beams" of positive significant correlation (at 95%) indicate comparable phase speed values of the waves for CLIPPER and the linear model and suggest that the parameterization of dissipation in the linear model was correctly tuned (see section 5.1.2). Note, however, that patches of significant negative correlation in the linear model have more zonal extension and smaller values than in CLIPPER, suggesting a different behavior for the wave reflection processes at the meridional boundaries and/or non linear processes acting in the OGCM run (see section 5).

[53] Considering the simplicity of the linear model compared to CLIPPER, the agreement between the two simulations is encouraging, with a comparable skill of the linear model to reproduce an OGCM simulation than in the equatorial Pacific [*Dewitte et al.*, 1999]. Nevertheless, knowing the differences between the tropical Pacific and Atlantic oceans, we speculate that the assumptions behind the linear formalism are less robust for the Atlantic. In order to verify that we remain in the frame work of linear theory,

Table 2. Comparison Between Observations (T/P+ERS, BL Currents) and the Linear Model Forced With Three Different Wind Products (ECMWF, ERS, and FSU) Over 1992–2000: RMS Difference (Correlation) in the ATL3@eq Region

		ECMWF	ERS	FSU
SLA	Mode2	1.53 (0.66)	1.54 (0.66)	1.52 (0.70)
	Mode1-6	1.52 (0.68)	1.53 (0.66)	1.30 (0.75)
ZCA	Mode2	8.49 (0.62)	9.05 (0.50)	8.78 (0.55)
	Mode 1–6	15.78 (0.63)	13.58 (0.58)	13.71 (0.59)

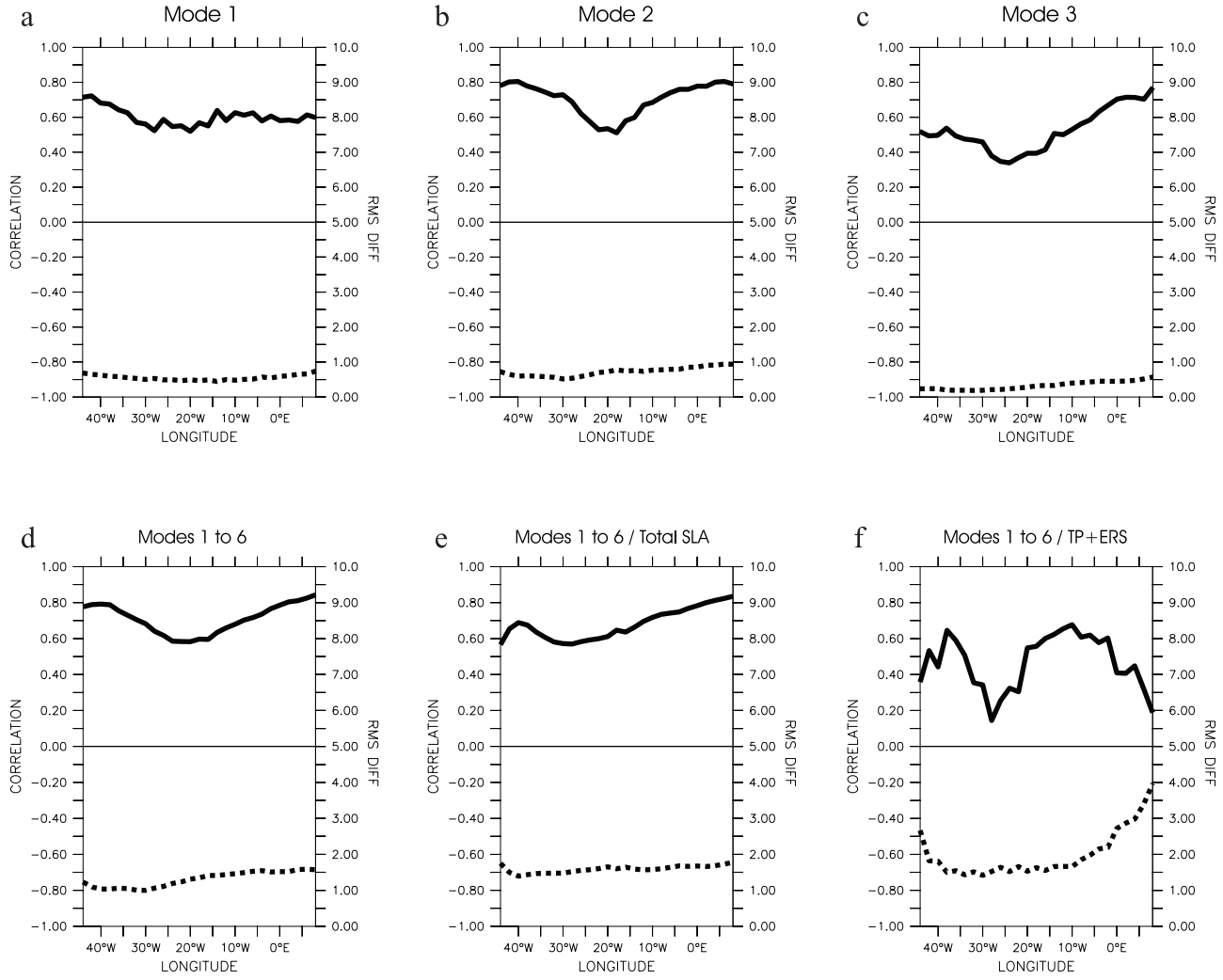

Figure 10. Plot of correlation (plain thick line) and RMS difference (dotted line) between CLIPPER and the linear model simulation for SLA, over 1981–2000, (a)–(c) for each contribution of the first three baroclinic modes and (d) for the summed-up contribution of the first six modes and (e) for the total SLA. Anomalies are relative to the seasonal cycle computed over 1981–2000. (f) The comparison between the total SLA from linear model and T/P+ERS is displayed (anomalies are relative to the seasonal cycle computed over 1993–1999). RMS is in cm.

non linear terms of the "full" u equation were estimated in CLIPPER (in particular, the terms $u_n \frac{\partial u_m}{\partial x}$, which "couple" the baroclinic modes). The results indicate that these quantities are always, at worst, one order of magnitude less than the rate of change of zonal current and wind-forcing terms. This provides further confidence in our analysis.

5. Reflection Efficiency of the Meridional Boundaries

[54] In the light of the previous results, it is likely that wave reflections occur at the African and Brazilian coasts (see Figure 7). This section proposes a methodology for estimating the reflection efficiency of the meridional boundaries for the long equatorial waves from the CLIPPER decomposition and the linear model.

[55] First, only the reflected contribution to the waves should be estimated. So that the locally wind forced component of the wave has to be removed, in order not to "contaminate" the reflected wave signal. An estimate of the contribution of local wind forcing to the wave amplitude was obtained by running the linear model with the wave reflections at the meridional boundaries cancelled (i.e., there is no contribution of reflected waves). The locally wind Kelvin (a^{wind}_{n,K^-}) and m meridional mode Rossby ($a^{wind}_{n,m}$) coefficients for each baroclinic mode are derived from this simulation and are removed from the reflected wave signal to estimate the part of the signal resulting from the wave reflection.

[56] As an illustration, Figure 13 presents the lag correlation between K and R_1 for the second baroclinic mode, which shows the consistency between the incident and reflected waves at the South America and African coasts. The broader zone of high correlation close to the eastern boundary suggests that wave reflection is more evident at the eastern boundary than at the western boundary. More-

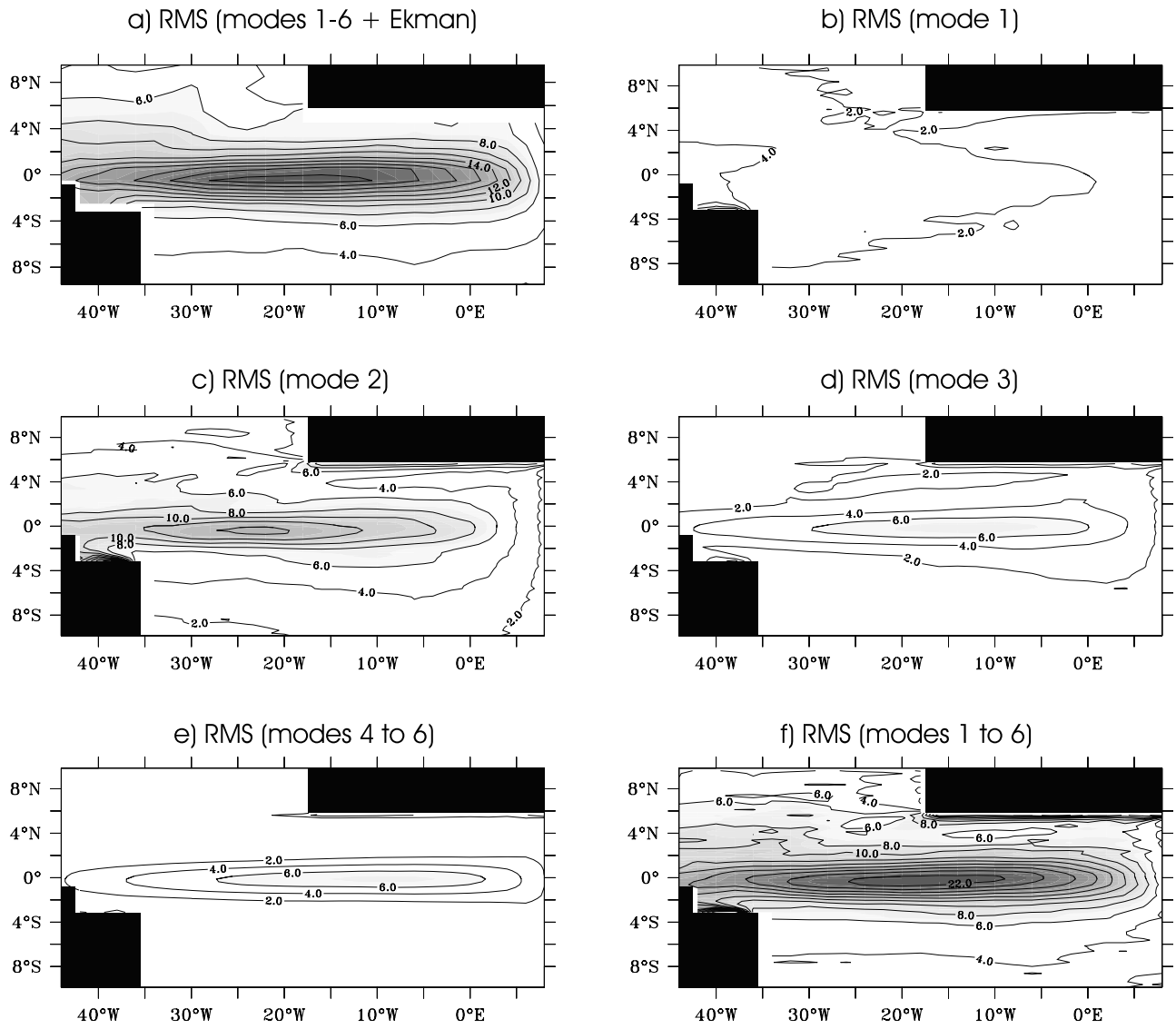

Figure 11. Same as Figure 1 but for the linear model simulation. Total ZCA for the linear model are derived from the summed-up contribution of the six first baroclinic modes and the Ekman currents.

over, the phase lag is coherent with the theoretical phase speeds and a reflection at the coast line.

[57] To estimate the reflection efficiency of the meridional boundary, we use the projection method described in CS79. We will review this theory to better understand the observed relationship between the Kelvin and the Rossby waves at the meridional boundaries.

5.1. Reflection at the Eastern Boundary

[58] To calculate the eastern boundary response, we use the condition that the zonal velocity is zero and that any incident Kelvin wave reflects into the Rossby waves, with a uniform height (in y) A_n at the eastern boundary: $a_{n,K-}\mathbf{M}_{n,K-} + \sum_{m=1}^{\infty} a_{n,m}\mathbf{R}_{n,m} = (0,\ 0,\ A_n)$, where $a_{n,K-}$ is the amplitude of the incident Kelvin waves and $a_{n,m}$ the amplitude of the mth meridional Rossby wave. (see notation in Appendix B). This equation is solved using the orthogonal properties of the eigenfunctions, as described in CS79.

[59] To estimate the reflection efficiency of the eastern meridional boundary, we compute the following quantity:

$$CE_{n,m}(x,t) = 100 \times \frac{\int_{YS}^{YN} \left(a_{n,m} - a_{n,m}^{wind}\right)(x, t + \delta t_{n,m}(x)).R_{n,m}^{u}(x,y)dy}{\int_{YS}^{YN} a_{n,K-}(x = 8^{\circ}E, t).\Psi_{n,K-}(x = 8^{\circ}E, y)dy},$$

where $R_{n,m}^{u}(y)$ ($\Psi_{n,K-}(y)$) is the horizontal structures of the m meridional Rossby (Kelvin) mode for the zonal velocity. $\delta t_{n,m}(x)$ is the time needed for the waves to travel from 8°E to the eastern meridional boundary (~10°E) as a nth baroclinic mode Kelvin wave and then, from the African coasts to the longitude x, as a nth baroclinic mode reflected mth-order Rossby wave. Note that, in the Gulf of Guinea, the wind variability is relatively low, which results in a weak sensitivity of our calculation to the estimate of $a_{n,K-}^{wind}$

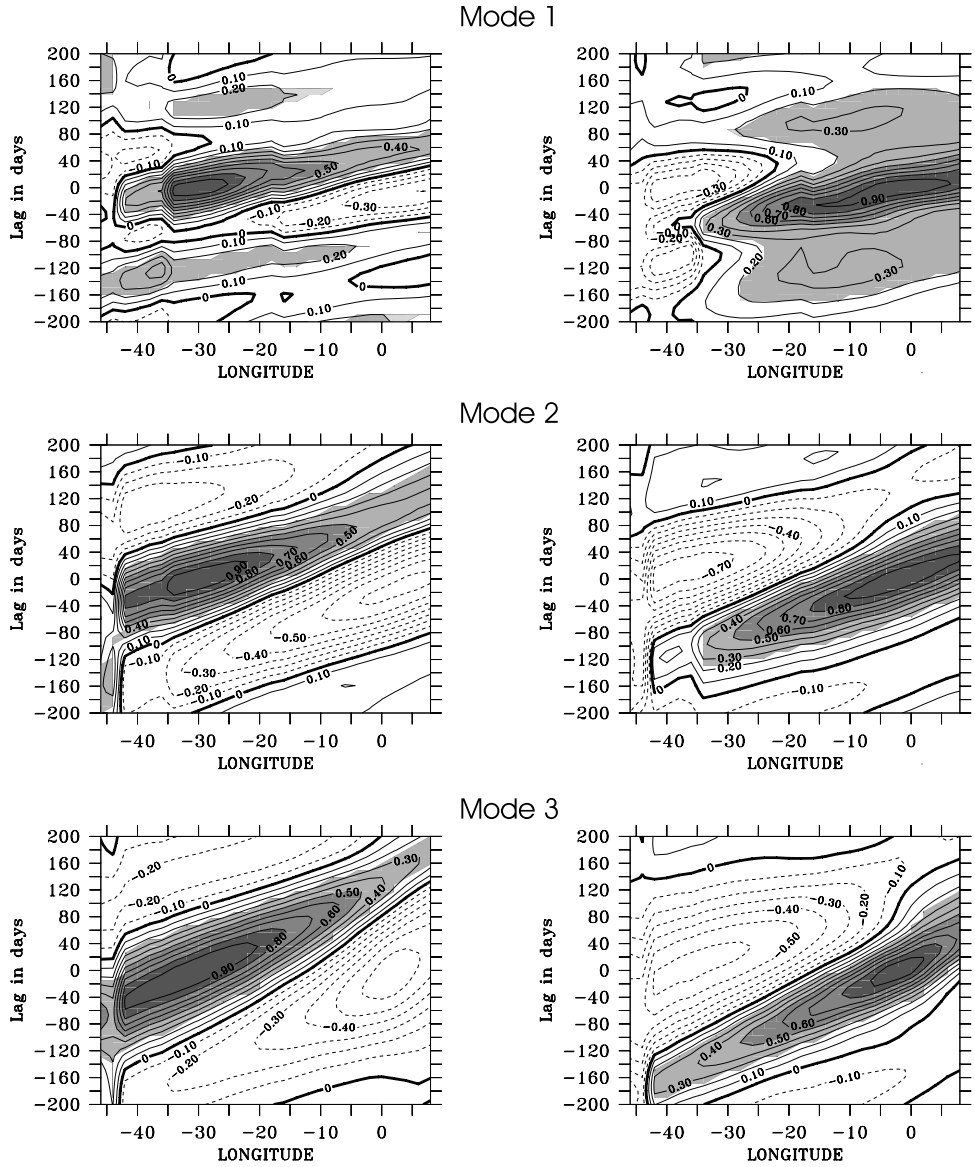

Figure 12. Same as Figure 8 but for the linear model.

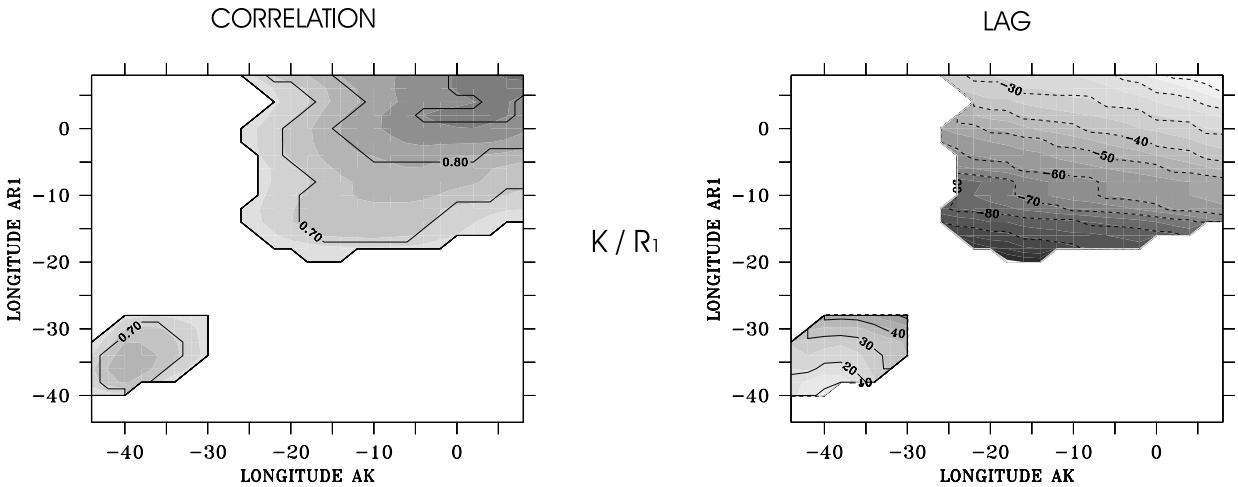

Figure 13. Lag correlation along the equator between K and R_1 coefficients for the second baroclinic mode: (left) correlation greater than 0.6 is represented (CI is 0.1) and (right) lag of maximum correlation is displayed (unit is days, and CI is 10 days).

Table 3. Percentage of the Incident Meridionally Integrated Zonal Mass Flux Due to Kelvin Waves That Reflects Into a Particular Meridional Rossby Wave (1–5) in the Infinite Meridional Case and in the Finite Meridional Case for the Baroclinic Modes 1, 2, and 6

	R_1	R_2	R_3	R_4	R_5
		Infinite Wall			
Baroclinic mode independent	50%	0%	12.5%	0%	6.3%
		Meridional Case			
Baroclinic mode 1	25.5%	3.81%	6.77%	3.74%	4.04%
Baroclinic mode 2	33.47%	2.05%	5.82%	1.48%	2.92%
Baroclinic mode 6	49.64%	0.00%	11.66%	0.01%	4.79%

and $a_{n,m}^{wind}$. $CE(x, t)$ is then time averaged is applied on (noted $\overline{CE}$), considering only Kelvin and Rossby coefficients larger than 10% of their respective RMS over the 1992–1999 period, in order to take into account the most significant reflections. $\overline{CE}$ then indicates the percentage of the incoming meridionally integrated zonal mass flux due to Kelvin waves that reflect into a particular meridional mode Rossby wave for a given baroclinic mode.

5.1.1. At the African Coast Line

[60] When $\overline{CE}$ ($x = 8°E$) is calculated with the infinite meridional functions (i.e., no longitudinal boundaries), the incident Kelvin waves reflect into symmetric Rossby waves with half of the incident meridionally integrated zonal mass flux being reflected in the first meridional Rossby mode and the remaining part spread over the higher-order meridional modes. Only symmetric Rossby waves are reflected by the incident Kelvin waves (Table 3). In the case of the meridionally bounded case, the amount returned by the reflected Rossby waves changes: the lower the order of baroclinic mode and the higher the order of meridional mode, the lesser the meridional scales are confined toward the equator, and the more the longitudinal boundaries impact the reflection of the Kelvin waves. For instance, for the second baroclinic mode (the most energetic), the linear theory using infinite meridional functions predicts that ~68.8% (Table 3) of the incident energy is reflected by the first five meridional Rossby waves, whereas the meridionally bounded case (i.e., taking into account the coastlines in the Gulf of Guinea) predicts only ~45,7%. Consequently, 23% of the incident energy is spread over the high-order meridional Rossby components. Moreover, a slight amount of the energy (3.5%) is now reflected onto the R_2 and R_4 Rossby waves.

[61] The results indicate that the African coasts behave almost as an infinite wall for the high-order baroclinic modes (order higher than 5) for the long equatorial waves (Table 3), since wave structures are hardly modified by the presence of the coasts near the equator.

[62] Considering that the R_1 reflected wave is the most energetic (as compared to higher-order meridional modes), a value for reflection efficiency of the eastern boundary can be estimated: considering only the first three most energetic baroclinic modes and their associated percentage of explained variance at the eastern boundary (see Figure 6), the calculation leads to a value for reflection efficiency of ~65% (of that of an infinite meridional wall).

5.1.2. Evolution Along the Propagation

[63] As the waves propagate westward, the decrease of $\overline{CE}(x)$ (Figure 14) indicates dissipation processes or vertically propagating energy: for baroclinic mode 3 (6), the reflection efficiency of the first meridional Rossby wave reaches 50% of its value at 8°E when estimated at 15°W (4°E). Note that for the first baroclinic mode, the reflection efficiency does not depend as much on the longitude as for the other modes: this is in agreement with a lesser sensitivity to dissipation processes for mode 1, than for modes 2 and 3 (due to a larger phase speed).

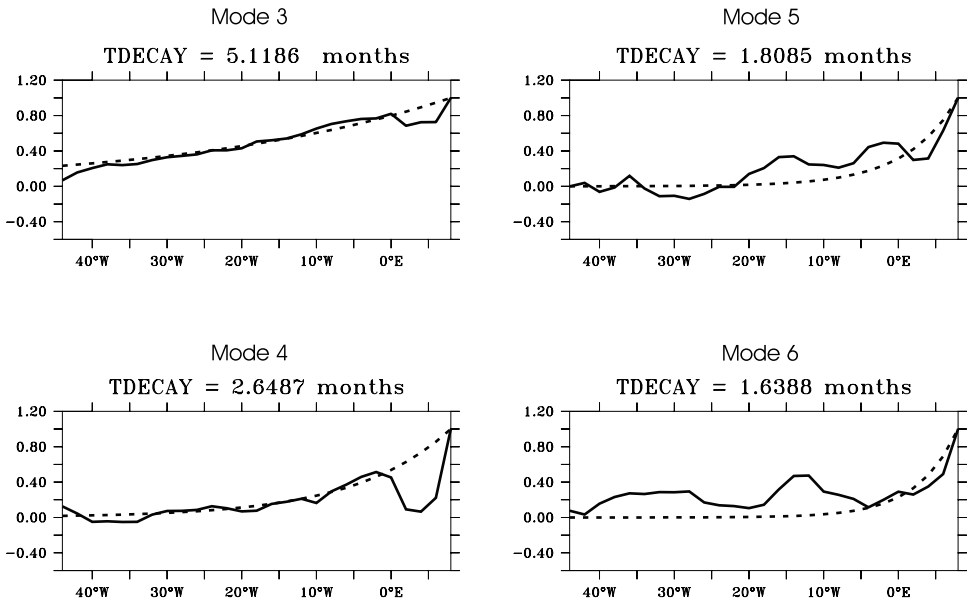

Figure 14. Plot of reflection efficiency at the eastern boundary ($\overline{CE}$) (solid line) as a function of longitude for baroclinic modes 3, 4, 5, and 6. The dotted line represents the least mean square best fit exponential curve to $\overline{CE}$. $\overline{CE}$ is adimensionalized by its value at 8°E.

[64] As a consistency check on our estimate of time decay for friction of the linear model and on the reflected wave coefficients derived from CLIPPER, the following simple calculation is carried out. It consists in comparing along the equator the results of the reflection efficiency at the African coast for CLIPPER and the one obtained assuming an incident K "fully" reflecting as a R_1, whose amplitude decreases exponentially with time as it propagates westward: $\exp(-(c_{n,R1} \times x)/r_n)$, where $c_{n,R1}$ is the speed value of the nth baroclinic mode R_1, taken as $c_n/3$, and r_n being the time decay value that is sought. Instead of considering meridional integrated flux as we have done earlier, the reflection efficiency factor is estimated at the equator so that we get: $CE_n(x, t) = \frac{\left(a_{n,1} - a_{n,1}^{wind}\right)(x, t+\delta t_n(x)).R_{n,1}^u(x)}{a_{n,K}(x=8°E,t).\Psi_{n,K}(x=8°E)}$ (see notation in Appendix B). The incoming K is normalized in order to have $CE_n(x = 8°E, t) = 1$ and a time averaging is also applied on $CE_n(x, t)$ (noted $\overline{CE_n}$).

[65] The results are displayed in Figure 14 for the best fit obtained with a least mean square minimization based method. Excluding regions where the exponential curve and model results do no match well, the results indicate that the decrease in amplitude of the Rossby wave can be modeled, to some extent, by a Rayleigh-type friction, with values for time decay of 5.12, 2.65, 1.81 and 1.64 months for modes 3 to 6 respectively. Assuming a relationship between time decay and phase speed that allows vertical separation of the type $r_n = r_1(c_n/c_1)^q$ [*Gent et al.*, 1983], we derive from the latter values: $r_1 = 27.57$ months and $q = 1.675$. This set of parameter that controls the magnitude of dissipation in the linear model was found to lead to the best comparison to CLIPPER for ZCA and SLA. Note that the linear model results are quite sensitive to these parameters. This is particularly important for the relative contribution of the baroclinic modes and the location of the variability peak in current and sea level anomalies. The larger q, the further east the variability maximum for total surface current anomalies, and the lesser the variability. We carried out two additional twin experiences with $q = 1$ and $q = 2$. The results of the comparison between the two simulations indicate that, for baroclinic mode 3 (6), the increase of q leads to an eastward shift of the location of the variability peak for ZCA of the order of 6° (9°) along with an average decrease of the variability by 38% (52%).

5.2. Reflection at the Western Boundary

[66] The western boundary response consists in a Kelvin wave and the short wavelength Rossby waves. Nevertheless, all the incident zonal mass flux is returned by the Kelvin waves (CS79):

$$\int_{YS}^{YN} a_{n,K^-}\Psi_{n,K^-}dy + \sum_{m=1}^{\infty}\int_{YS}^{YN} a_{n,m}\mathrm{R}_{n,m}^u dy = 0.$$

(see notation in Appendix B). In the finite meridional case (CS79), there is no analytical solution to this equation, as was the case in the infinite meridional case (CS77), because there are no longer symmetric properties of the horizontal structures of the Kelvin and Rossby waves with respect to the equator (Figure B1). This implies that, one cannot derive unambiguously the contribution of a specific incident meridional Rossby mode to the reflected Kelvin mode. We define the reflection efficiency at the western boundary as follows:

$$CW_n(x,t) = 100 \times \sum_{m=1}^{M} \frac{a_{n,m}(x',t) \times \int_{YS}^{YN} R_{n,m}^u(x',y)dy}{\left(a_{n,K^-} - a_{n,K-}^{wind}\right)(x, t+\delta t_{n,m}(x,x')) \times \int_{YS}^{YN} \Psi_{n,K}(x,y)dy},$$

where $\delta t_{n,m}(x, x')$ is the time needed for the waves to travel westward from the longitude x' to the western boundary as a nth baroclinic mode waves and then from the South American coast to the longitude x as a reflected nth baroclinic mode Kelvin wave. As before, $a_{n,K-}^{wind}$, the locally wind-forced contribution to the Kelvin wave for the *nth* baroclinic mode, is derived from the linear model simulation and a time averaging is applied on $CW(x, t)$ (noted $\overline{CW}$). Thus, with such a definition, if all the incoming Rossby waves reflect as Kelvin waves (without "loss" of energy) at the western boundary, $\overline{CW_n}(x)$ should be close to 100% at the South American coast. Several tests have been carried out, including sensitivity experiments on the way the local wind contribution to the Kelvin wave is estimated from the linear model and on the number of meridional Rossby modes retained (M) in the calculation. We found values in the 10 to 60% range for the first 3 baroclinic modes, for $x' = 37°$W and $x = 44°$W (i.e., close to the Brazilian coast). $\overline{CW_n}(x)$ generally undergoes a sharp decrease in amplitude when the reference for the Kelvin wave amplitude is taken further from the coast (i.e., increased x). West of 37°W, $\overline{CW_n}(x)$ also decreases sharply. These results indicate that wave reflection does take place at the western boundary, but that it is altered by some processes, which includes the nonlinear interactions with the western boundary current system, nonlinear dissipation, the more complicated than modeled coastline and bottom topography, as well as the presence of short Rossby waves or short spatial scale wind forcing.

[67] To summarize, although reflection efficiency is difficult to quantify because of the presence of coasts near the equator, the relatively good agreement between CLIPPER and the linear model simulation (section 4) in which wave reflections take place with a 100% efficiency suggests that a large amount of the incoming Rossby wave variability is returned as Kelvin wave variability. In particular, canceling the western boundary reflection in the linear model, degrades the comparison with CLIPPER. For instance, for total SLA, the correlation (RMS difference) between CLIPPER and the linear model at [40°W, 0°N] is 0.69 (1.5 cm) and 0.54 (1.75 cm), with and without western boundary reflections respectively.

6. Discussion and Conclusion

[68] A high-resolution OGCM simulation is used to study the equatorial waves in the tropical Atlantic in 1981–2000. We first investigated the baroclinic modes contribution to the surface zonal current and sea level variability at interannual timescales. The second baroclinic mode is the most energetic. The first and the third modes contribute with comparable amplitude but with different spatial distribution in the equatorial waveguide. The first mode exhibits a

variability peak in the western part of the basin, where the maximum zonal wind stress variability is observed, whereas the energy of the third baroclinic mode is confined in the east, where the largest zonal gradients in the density field and in the vertical mode characteristics are found. The summed-up contribution of the higher-order (4–6) baroclinic modes variability is as energetic as the two gravest modes and is largest in the east. Despite the too deep and too diffuse thermocline in comparison to the observations, the energy distribution on the baroclinic modes presented in this study is believed to share many characteristics to the one taking place in the tropical Atlantic. At the moment, the relative scarcity of observed data in the tropical Atlantic does not allow for a similar calculation of the baroclinic mode variability, especially in terms of ZCA. Nevertheless, our diagnostic applied to other OGCM simulations, indicates that it is a robust feature. In particular, at the early stage of the study, we used an OGCM simulation in which temperature profiles were assimilated [*Masina et al.*, 2001] and comparable results were derived. How model characteristics (vertical resolution, diffusion.) and variability alter our results on the relative contribution of the baroclinic modes, remains to be further investigated as more realistic simulation of the tropical Atlantic and more data become available.

[69] Kelvin and meridional Rossby components were then derived for each of the gravest baroclinic mode contribution by projecting onto the associated meridional structures. The effect of boundaries close to the equator is taken into consideration. It is shown to impact wave coefficients near the meridional boundaries, as compared to the simplified case that assumes infinite meridional extension basin (CS77). We find evidence of equatorial Kelvin and Rossby waves propagation with phase speed values close to theoretical ones. The results are compared to the results of a multimode linear simulation using the projection coefficients and phase speed values derived from the OGCM simulation. Dissipation in the linear model is modeled as a Rayleigh-type friction. It is tuned in order to fit the decrease in amplitude of the Rossby waves of the OGCM as they propagate westward from the eastern boundary. The comparison suggests that not only long equatorial wave propagations should be observable in the equatorial Atlantic, but that these waves explain a large part of the interannual variability and have an important role in the adjustment of the tropical Atlantic Ocean to the wind forcing. In addition, wave reflections have been identified in the OGCM. A 65% reflection efficiency is estimated at the eastern boundary whereas at the western boundary, the reflection is less clear, possibly because of the interaction with western boundary currents and the difficulty to separate the different baroclinic mode contributions.

[70] The present study points out to the necessity of taking into account the variability in the vertical structure when interpreting surface observations, since the energy is distributed over a large number of baroclinic modes. In particular, this raises the issue of whether or not vertically propagating energy takes place in the equatorial Atlantic at interannual timescales. Our results suggest that substantial energy flux associated to surface forcing reaches the subthermocline in the OGCM: For instance, a spectral analysis (FFT) of the wind stress forcing in the central basin exhibits a peak of energy at the 16-month period, similar to what is found in SST in the ATL3 region. At this frequency, an harmonic analysis highlights clear vertical propagating energy path in agreement with the theoretical WKB first Rossby ray path (not shown). Also, note that propagation at interannual timescales have not yet been clearly evidenced from the TOPEX/POSEIDON sea level data [*Handoh and Bigg*, 2000]. Our work calls for further investigation of model outputs and/or assimilated products in order to study the mechanisms of wave dissipation in the tropical Atlantic.

[71] At last, we believe that the good skill of the linear model to reproduce the equatorial interannual variability of the OGCM is encouraging for the understanding of the low-frequency equatorial Atlantic variability, and especially the zonal equatorial mode. The level of agreement between the two models is similar to what is found in the tropical Pacific as far as the dynamical fields are concerned [cf. *Dewitte et al.*, 1999] and preliminary results with the linear model of the tropical Atlantic indicate that SST variability is well reproduced from a simple thermodynamical model that considers anomalous advection of mean temperature induced by the waves in a 35 m depth mixed layer. In particular, an EOF analysis on these simulated SSTAs reveals a structure similar to the observed zonal equatorial mode (not shown). This is promising for future simple coupled modeling work in the tropical Atlantic sector [cf. *Zebiak*, 1993]. There are of course larger limitations of such approach as compared to the Pacific considering the higher connection between the equatorial and the off equatorial variability in the Atlantic. The interaction with the seasonal cycle has also to be adequately considered. Despite these differences with the Pacific, our results suggest that mechanisms involving equatorial wave propagations like the delayed action oscillator and/or the zonal active feedback [*Picaut et al.*, 1997] that control the low-frequency coupled variability in the tropical Pacific, are potentially acting in the tropical Atlantic. To investigate this issue, one first needs to quantify the contribution of the horizontal and vertical advection induced by equatorial waves to the changes in SST. This is work under progress.

Appendix A: Influence of Temporal Variability in the Stratification on the Baroclinic Mode Contributions

[72] The baroclinic mode contributions to zonal current and pressure anomalies are estimated in three different ways: the estimation depends on how the stratification is allowed to evolve in time: First, the vertical structures are derived from the mean stratification (method $\bar{t}$). Second, the seasonal cycle in temperature and salinity is considered (method t_{12}), third, the instantaneous density profiles are used to derive the vertical functions F_n (method t).

A1. Impact on CLIPPER Vertical Decomposition

[73] Results are presented in Figure A1 as RMS difference maps for ZCA. The benchmark is the result of the projection on the steady vertical functions. On the left panels, maps of RMS difference between method $\bar{t}$ and method t are presented for the first four baroclinic modes. They show significant differences with the decomposition for which the temporal variability in N^2 is retained (method t). The RMS difference is of the order

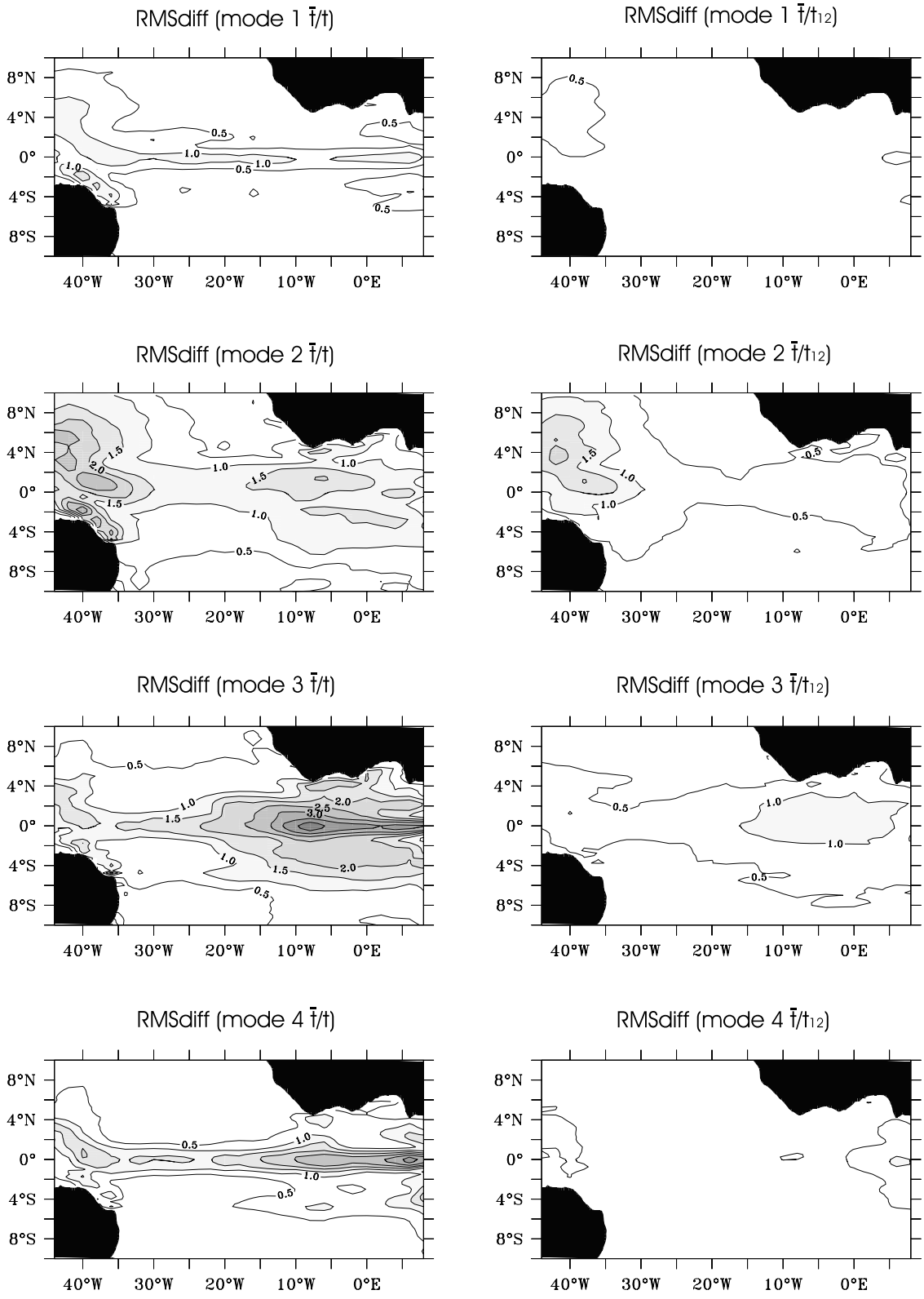

Figure A1. Map of RMS difference for CLIPPER ZCA (left panels) between the results of method $\bar{t}$ and method t and (right panels) between the results of method $\bar{t}$ and method t_{12} for the four gravest baroclinic modes over 1981–2000. Anomalies are relative to the seasonal cycle computed over 1981–2000. Unit is cm s^{-1}. Contour interval is 0.5 cm s^{-1}. Values larger than 6 cm s^{-1} are shaded.

of 2 cm s^{-1} for modes 1, 2, and 4 on average over the basin. The baroclinic mode 3 exhibits a maximum RMS difference of 4 cm s^{-1} around 7°W at the equator. The differences are more important for modes 5 and 6 (6 cm s^{-1}). This illustrates the large variability of thermocline depth and its impact on the baroclinic mode contributions. Results of method t are, however, difficult to interpret within linear theory, which assumes a steady density background. It is indeed likely that a large part of the variability associated with rapid (relative to the low-frequency motion that we are considering in this study, i.e., interannual propagating waves) changes in the thermal structure is associated with nonlinear processes, which include modal dispersion induced by temporal change in the background stratification. This is consistent with the results of method t_{12} which show smaller differences with method $\bar{t}$ (Figure A1, right panel), than method t (compared to method $\bar{t}$). The seasonal dependence impacts the gravest baroclinic modes 1, 2, and 3 with RMS differences of the order of 0.5–1 cm s^{-1} The largest differences are found for mode 2, in particular in the western part of the basin where the differences are of the order of the one observed between method $\bar{t}$ and method t (>2 cm s^{-1}). For the high-order baroclinic modes the difference is weak.

[74] Because of the marked seasonal cycle of the thermocline depth [*du Penhoat and Treguier*, 1985], the wind projection coefficients exhibit significant seasonal variations as illustrated in Figure A2, which displays the seasonal cycle of P_n for the first six baroclinic modes, (to be evaluated along with Figure 9). Whereas P_1 varies by as much as 30% from winter to summer, P_3 varies by up to 100%. The shoaling of the thermocline in summer (July–August) leads to weaker value for P_1 and larger values for P_3. P_2 has the weakest variations whereas P_6 presents a marked semi annual cycle consistently with the high frequency projecting preferentially on the higher-order modes. These seasonal variations are larger than the interannual variations for mode 1, 3, and 5, and are of the same order of magnitude than the interannual variations for mode 2 and 4 (see Table A1). Considering the magnitude of the seasonal cycle in P_n, these variations are taken into account in the linear model simulation.

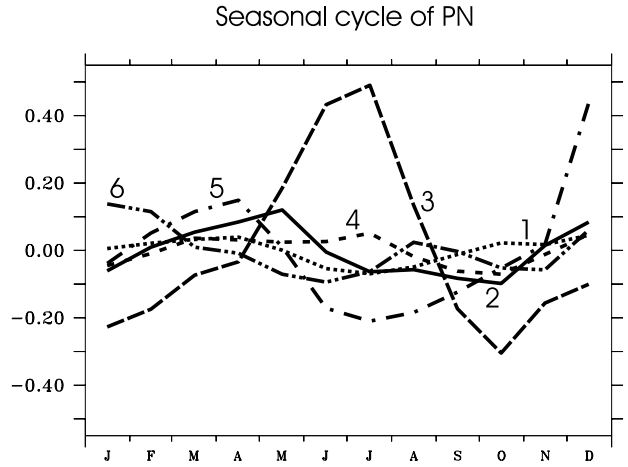

Figure A2. Seasonal variation of the wind projection coefficient of the linear model for the first six baroclinic modes in the ATL3@EQ region.

Table A1. Seasonal and Interannual Variability (RMS) of the Wind Stress Coefficients P_n for the Six First Baroclinic Modes

	Order of the Baroclinic Mode					
	1	2	3	4	5	6
Seasonal variability (RMS)	0.042[a]	0.075	0.236[a]	0.054	0.197[a]	0.090[a]
Interannual variability (RMS)	0.027	0.081[a]	0.147	0.059[a]	0.117	0.077

A2. Impact on the Linear Model Results

[75] When the longitudinal variation of the wind projection coefficients is taken into account in the linear model, the zone of maximum variability (RMS) of the summed-up contribution of modes 1 to 6 to ZCA is shifted eastward in longitude by ∼15°, in better agreement with the CLIPPER decomposition. Differences are largest for the high-order baroclinic modes. This shift of the spatial structure of the variability maps is associated with lower RMS variability for each baroclinic mode, compared to the run using $\overline{N^2(x = 14°W)}$. With the wind projection coefficients, for which the seasonal and longitudinal variability in P_n is retained, the linear model reproduces better the spatial structure of variability maps (RMS) of CLIPPER. The results show that the seasonal dependency of P_n impacts the high-order baroclinic modes (3–6) with an eastward shift of the zone of maximum variability of the order of 2°–3°, compared to the model run without the seasonal dependency of P_n. Correlation (RMS difference) between CLIPPER and the linear model for the summed-up contribution to SLA of the six first baroclinic modes is increased (decreased) by 0.1 (0.5 cm) on average along the equator when considering the seasonal dependence of P_n. In addition, these parameterizations of the linear model yield to better agreement with the altimetric observations (Table A2).

Appendix B: Horizontal Mode Decomposition

B1. Equation of the Meridional Velocity and Its Solutions

[76] We are looking for the solutions of the linearized equations of the movement, as free waves: $q_n = Q_n(y) \times e^{i(k_n x - \omega_n t)}$, with q being u, v, or h. This leads us to solve the differential equation for the meridional velocity:

$$v_{yy} + \left(\omega^2 - k^2 - k/\omega - y^2\right)v = 0. \tag{B1}$$

This equation is solved for low-frequency long waves.

[77] In the tropical Pacific Ocean, for simplicity, this equation is usually solved without longitudinal boundaries: it is the infinite meridional expansion case of *Cane and*

Table A2. Comparison Between Observations (T/P+ERS, BL Currents) and the Linear Simulation (Summed-Up Contribution of Modes 1–6) Forced With ECMWF Over 1992–2000 for the Runs Using $\overline{P_n(x = 14°W)}$, $\overline{P_n(x)}$, and P_n (x, t_{12}): RMS Difference (Correlation) in the ATL3 Region

	$\overline{P_n(x = 14°W)}$	$\overline{P_n(x)}$	$P_n(x, t_{12})$
SLA	1.42 (0.68)	1.3 (0.70)	1.29 (0.71)
ZCA	12.74 (0.52)	11.33 (0.60)	10.17 (0.59)

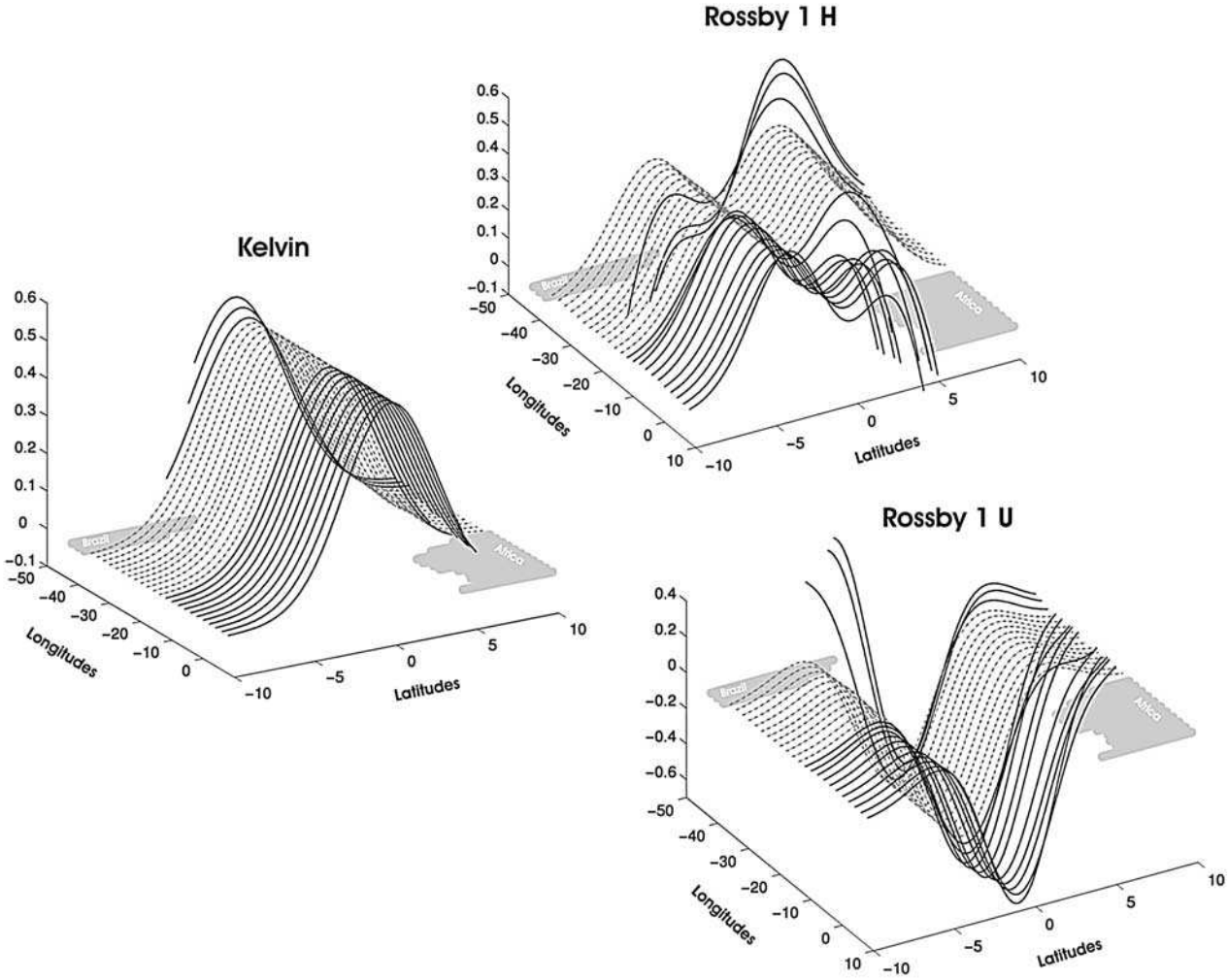

Figure B1. Horizontal structures associated with the (left) K and (right) R_1 (pressure structure is displayed on top, and zonal current structure is displayed at the bottom) as a function of longitude and latitude. The solid curves correspond to structures modified by the presence of the coasts near the equator, whereas the dashed curves have the structure of the infinite meridional case (see text).

Sarachik [1977] (hereinafter referred to as CS77). In the tropical Atlantic, the presence of longitudinally varying boundaries close to the equator in the Gulf of Guinea and near the South America coasts imposes new boundary conditions:

$$v(y) = 0 \tag{B2}$$

at Y_S and Y_N, Y_S and Y_N being the southern and the northern boundary respectively. The complete calculus is presented by CS79. The key steps of this calculation are briefly recalled below.

[78] The eigenvalues μ_m of the dispersion equation verify that: $\omega_m^2 - k^2 - k/\omega_m = 2\mu_m + 1$, $m = 0, 1, 2, \ldots, \infty$. In the case of low-frequency long waves, it simplifies as

$$-k/\omega_m = 2\mu_m + 1 \tag{B3}$$

[79] The solution to equation (B1) for the low-frequency long wavelength approximation is

$$v(y) = U\left(-\mu_m - 1/2, \sqrt{2}y\right) + bV\left(-\mu_m - 1/2, \sqrt{2}y\right), \tag{B4}$$

[80] U and V being the parabolic cylinder functions, in the notation of *Abramowitz and Stegun* [1965] (equation (B4)). The parameters b and μ_m are determined using equation (B2).

[81] First, using the boundary condition (B2) at Y_N, we find:

$$b = -\frac{U\left(-\mu_m - 1/2, \sqrt{2}Y_N\right)}{V\left(-\mu_m - 1/2, \sqrt{2}Y_N\right)} \tag{B5}$$

[82] Then, applying the boundary condition (B2) at Y_S yields to an equation for μ_m (this equation is solved numerically):

$$U\left(-\mu_m - 1/2, -\sqrt{2}|Y_s|\right) - \frac{U\left(-\mu_m - 1/2, \sqrt{2}Y_N\right)}{V\left(-\mu_m - 1/2, \sqrt{2}Y_N\right)} \cdot V\left(-\mu_m - 1/2, -\sqrt{2}|Y_s|\right) = 0. \tag{B6}$$

[83] The eigenfunctions $v(y)$ form a complete orthogonal basis. For each baroclinic mode, a normalized version of these functions is defined as:

$$\Psi_{n,m}(y) = v_{n,m}(y) \cdot \left[\int_{Y_S}^{Y_N} v_{n,m}^2(y) \, . \, dy \right]^{-1/2} . \tag{B7}$$

[84] Note that when Y_S and Y_N tend to the infinite, these functions tend to the well known complete basis of the Hermite functions established in the infinite meridional case.

B2. Complete Basis of Long-Wavelength Meridional Modes

[85] For each baroclinic mode (n), the Kelvin ($-$) and anti-Kevin ($+$) meridional structures are defined as:

$$\mathbf{M}_{n,K}^{\pm} = 2^{-1/2} \begin{bmatrix} \Psi_{n,K}^{\pm} \\ 0 \\ \mp\Psi_{n,K}^{\pm} \end{bmatrix} \text{ with } \Psi_K^{\pm}(y) = e^{\pm y^2/2} \times \left[\int_{Y_S}^{Y_N} e^{\pm y^2} dy \right]^{-1/2} . \tag{B8}$$

A vector which has $v = 0$ and whose u and h components are proportional to the Rossby waves is defined as:

$$\mathbf{R}_{n,m}(y) = \begin{bmatrix} R_{n,m}^u \\ 0 \\ R_{n,m}^h \end{bmatrix} = \frac{1}{4\mu_{n,m}(\mu_{n,m}+1)} \begin{bmatrix} -(2\mu_{n,m}+1).\Psi'_{n,m}(y) + y\Psi_{n,m}(y) \\ 0 \\ (2\mu_{n,m}+1).y\Psi_{n,m}(y) + \Psi'_{n,m}(y) \end{bmatrix} . \tag{B9}$$

[86] $R_{n,m}^u(y)$ and $R_{n,m}^h(y)$ are the horizontal structures of the m meridional Rossby mode for the zonal velocity and the sea level, respectively.

[87] In order to estimate the contribution of the different meridional modes (m), both pressure and zonal current anomaly contributions are projected onto the complete basis of long-wavelength meridional modes:

$$\begin{pmatrix} u_n \\ 0 \\ p_n \end{pmatrix} = a_{n,K^\pm}\mathbf{M}_{n,K^\pm} + \sum_{m=1}^{\infty} a_{n,m}\mathbf{R}_{n,m} \text{ with } a_{n,K^\pm}$$

$$= \int_{Y_S}^{Y_N} \mathbf{M}_{n,K^\pm} \bullet \begin{pmatrix} u_n \\ \\ p_n \end{pmatrix} .dy \; a_{n,m} = \int_{Y_S}^{Y_N} \mathbf{R}_{n,m} \bullet \begin{pmatrix} u_n \\ \\ p_n \end{pmatrix} .dy \tag{B10}$$

[88] The meridional structures for the Kelvin (K) mode and the first Rossby mode (R_1) are presented in Figure B1 for the second baroclinic mode: there are no longer symmetric properties of the horizontal structures of the Kelvin and Rossby waves with respect to the equator.

[89] **Acknowledgments.** We are grateful to Sylvain Michel, A. M. Treguier, and the whole CLIPPER project team for the model outputs so kindly provided. We also thank the CERSAT and AVISO for the altimetric data. Fruitful discussions with Simona Masina were very helpful at the early stage of this study. We would also like to acknowledge Eric Greiner and Jean-Marc Molines for their help in computing the sea surface height. Part of this work was performed while the main author visited IRD-Nouméa for 5 months. Christian Colin (director of IRD-Nouméa) and Yves Gouriou were very instrumental in facilitating this stay. Finally, the main author wishes to thank her family and, in particular, Anthony Thevenin for their encouragement during the course of this study.

References

Abramowitz, M., and I. A. Stegun (1965), *Handbook of Mathematical Functions*, 1046 pp., Dover, Mineola, N. Y.

Arhan, M., H. Mercier, B. Bourles, and Y. Gouriou (1998), Hydrographic sections across the Atlantic at 7°30N and 4°30S, *Deep Sea Res., Part I*, *45*, 829–872.

Arnault, S. (1987), Tropical Atlantic geostrophic currents and ship drifts, *J. Geophys. Res.*, *92*, 5076–5088.

Arnault, S., Y. Menard, and J. Merle (1990), Observing the tropical Atlantic Ocean in 1986–1987 from altimetry, *J. Geophys. Res.*, *95*, 17,921–17,945.

Atlas, R., R. Hoffman, S. Bloom, J. Jusem, and J. Ardizzone (1996), A multi-year global surface wind velocity data set using SSM/I wind observations, *Bull. Am. Meteorol. Soc.*, *77*, 869–882.

Barnier, B., and the CLIPPER Project Team (2000), 1/6° reference experiment, 1/6 Atlantic circulation model forced by the ECMWF climatology: Preliminary results, *LEGI Rep. CLIPPER-R2-2000*, Lab. des Ecoulements Géophys. Industriels, Grenoble, France. (Available as www.ifremer.fr/lpo/clipper)

Barnier, B., L. Siefridt, and P. Marchesiello (1995), Thermal forcing for a global ocean circulation model using a three-year climatology of ECMWF analyses, *J. Mar. Syst.*, *6*, 363–380.

Bentamy, A., Y. Quilfen, F. Gohin, N. Grima, M. Lenaour, and J. Servain (1996), Determination and validation of average wind fields from ERS-1 scatterometer measurements, *Global Atmos. Ocean Syst.*, *4*, 1–29.

Blanke, B., and P. Delecluse (1993), Variability of the tropical Atlantic Ocean simulated by general circulation model with two mixed layer physics, *J. Phys. Oceanogr.*, *23*, 1363–1388.

Blumenthal, M. B., and M. A. Cane (1989), Accounting for parameter uncertainties in model verification: An illustration with tropical sea surface temperature, *J. Phys. Oceanogr.*, *19*, 815–830.

Bonjean, F., and G. S. E. Lagerloef (2002), Diagnostic model and analysis of the surface currents in the tropical Pacific Ocean, *J. Phys. Oceanogr.*, *32*, 2938–2954.

Bretherton, F. P., R. E. Davis, and C. B. Fandry (1976), A technique for objective analysis and design oceanographic experiments applied to mode-73, *Deep Sea Res.*, *23*, 559–582.

Cane, M. A., and R. J. Patton (1984), A numerical model for low frequency equatorial dynamics, *J. Phys. Oceanogr.*, *14*, 1853–1863.

Cane, M. A., and E. S. Sarachik (1977), Forced baroclinic ocean motions. II. The linear equatorial bounded case, *J. Mar. Res.*, *35*, 375–432.

Cane, M. A., and E. S. Sarachik (1979), Forced baroclinic ocean motions. III: The linear equatorial basin case, *J. Mar. Res.*, *37*, 355–398.

Carton, J. A., and B. Huang (1994), Warm events in the tropical Atlantic, *J. Phys. Oceanogr.*, *24*, 888–903.

Chang, P., L. Ji, and H. Li (1997), A decadal climate variation in the tropical Atlantic Ocean from thermodynamics air-sea interactions, *Nature*, *385*, 516–518.

Delecluse, P., J. Servain, C. Levy, K. Arpe, and L. Bengtsson (1994), On the connection between the 1984 Atlantic warm event and the 1982–83 ENSO, *Tellus, Ser. A*, *46*, 448–464.

Dewitte, B., G. Reverdin, and C. Maes (1999), Vertical structure of an OGCM simulation of the tropical Pacific Ocean in 1985–1994, *J. Phys. Oceanogr.*, *30*, 1562–1581.

Dewitte, B., S. Illig, L. Parent, Y. duPenhoat, L. Gourdeau, and J. Verron (2003), Tropical Pacific baroclinic mode contribution and associated long waves for the 1994–1999 period from an assimilation experiment with altimetric data, *J. Geophys. Res.*, *108*(C4), 3121, doi:10.1029/2002JC001362.

du Penhoat, Y., and Y. Gouriou (1987), Hindcasts of equatorial sea surface dynamic height in the Atlantic in 1982–1984, *J. Geophys. Res.*, *92*, 3729–3740.

du Penhoat, Y., and A.-M. Treguier (1985), The seasonal linear response of the Atlantic Ocean, *J. Phys. Oceanogr.*, *15*, 316–329.

du Penhoat, Y., M. A. Cane, and R. J. Patton (1983), Reflections of low frequency equatorial waves on partial boundaries, in *Hydrodynamics of the Equatorial Ocean*, edited by J. C. J. Nihoul, pp. 237–258, Elsevier Sci., New York.

Enfield, D. B., and D. A. Mayer (1997), Tropical Atlantic sea surface temperature variability and its relation to El Niño-Southern oscillation, *J. Geophys. Res.*, *102*, 929–945.

Gent, R. G., K. O'Neill, and M. A. Cane (1983), A model of the semiannual oscillation in the equatorial Indian Ocean, *J. Phys. Oceanogr.*, *13*, 2148–2160.

Gouriou, Y., et al. (2001), Deep circulation in the equatorial Atlantic Ocean, *Geophys. Res. Lett.*, *28*, 819–822.

Handoh, I. C., and G. R. Bigg (1995), A self-sustaining climate mode in the tropical Atlantic, 1995–97: Observations and modelling, *Q. J. R. Meteorol. Soc.*, *126*, 807–821.

Hisard, P. (1980), Observation de réponses de type "El Niño" dans l'Atlantique tropical oriental-Golfe de Guinée, *Oceanol. Acta*, *3*, 69–78.

Lagerloef, G. S. E., G. T. Mitchum, R. B. Lukas, and P. P. Niiler (1999), Tropical Pacific near-surface currents estimated from altimeter, wind, and drifter data, *J. Geophys. Res.*, *104*, 23,313–23,326.

Le Traon, P. Y., F. Nadal, and N. Ducet (1998), An improved mapping method of multi-satellite altimeter data, *J. Atmos. Oceanic Technol.*, *15*, 522–534.

Levitus, S., T. P. Boyer, M. E. Conkright, T. O'Brien, J. Antonov, C. Stephens, L. Stathoplos, D. Johnson, and R. Gelfeld (1998), *World Ocean Database 1998*, vol. 1, *Introduction, NOAA Atlas NESDIS 18*, Natl. Oceanic and Atmos. Admin., Silver Spring, Md.

Madec, G., P. Delecluse, M. Imbard, and C. Levy (1998), OPA 8.1 general circulation model reference manual, *Notes IPSL*, *11*, 91 pp.

Marin, F., and Y. Gouriou (2000), Heat fluxes across 7°30′N and 4°30′S in the Atlantic Ocean, *Deep Sea Res., Part I*, *47*, 2111–2139.

Masina, S., N. Pinardi, and A. Navarra (2001), A global ocean temperature and altimeter data assimilation system for studies of climate variability, *Clim. Dyn.*, *17*, 687–700.

Mellor, J. L., and X.-H. Wang (1996), Pressure compensation and the bottom boundary layer, *J. Phys. Oceanogr.*, *26*, 2214–2222.

Merle, J. M., M. Fieux, and P. Hisard (1980), Annual signal and interannual anomalies of sea surface temperatures in the eastern equatorial Atlantic Ocean, *Deep Sea Res.*, *26*, suppl. II–V, 77–102.

Millero, F. J., and A. Poisson (1981), International one-atmosphere equation of state of seawater, *Deep Sea Res., Part A*, *28*, 625–629.

Nobre, P., and J. Shukla (1996), Variations of sea surface temperature, wind stress, and rainfall over the tropical Atlantic and South America, *J. Clim.*, *9*, 2464–2479.

Philander, S. G. H. (1978), Forced oceanic waves, *Rev. Geophys.*, *16*, 15–46.

Philander, S. G. H. (1986), Unusual conditions in the tropical Atlantic Ocean in 1984, *Nature*, *322*, 236–238.

Picaut, J., J. Servain, A. J. Busalacchi, and M. Seva (1984), Interannual variability versus seasonal variability in the tropical Atlantic, *Geophys. Res. Lett.*, *11*, 787–790.

Picaut, J., F. Masia, and Y. du Penhoat (1997), An advective-reflective conceptual model for the oscillatory nature of the ENSO, *Science*, *277*, 663–666.

Rajagopalan, B., Y. Kishnir, and Y. M. Tourre (1998), Observed midlatitude and tropical Atlantic climate variability, *Geophys. Res. Lett.*, *25*, 3670–3967.

Reynaud, T., P. Legrand, H. Mercier, and B. Barnier (1998), A new analysis of hydrographic data in the Atlantic and its application to an inverse modelling study, *Int. WOCE Newsl.*, *32*, 29–31.

Reynolds, R. W., and T. M. Smith (1994), Improved global sea surface temperature analyses using optimum interpolation, *J. Clim.*, *7*, 929–948.

Richardson, P. L., and T. K. McKee (1984), Average seasonal variation of the Atlantic North Equatorial Countercurrent from ship drift data, *J. Phys. Oceanogr.*, *14*, 1226–1238.

Sciremammano, F., Jr. (1979), A suggestion for the presentation of correlations and their significance, *J. Phys. Oceanogr.*, *9*, 1273–1276.

Servain, J. (1991), Simple climatic indices for the tropical Atlantic Ocean and some applications, *J. Geophys. Res.*, *96*, 15,137–15,146.

Servain, J., J. N. Stricherz, and D. M. Legler (1997), *TOGA Pseudo-Stress Atlas 1985–1994*, vol. I, *Atlantic Ocean*, 158 pp., Florida State Univ., Tallahassee.

Servain, J., I. Wainer, J. P. McCreary, and A. Dessier (1999), Relationship between the equatorial and meridional modes of climatic variability in the tropical Atlantic, *Geophys. Res., Lett.*, *26*, 485–488.

Servain, J., I. Wainer, H. L. Ayina, and H. Roquet (2000), The relationship between the simulated climatic variability modes of the tropical Atlantic, *Int. J. Climatol.*, *20*, 939–953.

Sutton, R. T., S. P. Jewson, and D. P. Rowell (2000), The elements of climate variability in the tropical Atlantic region, *J. Clim.*, *13*, 3261–3284.

Tourre, Y., B. Rajagopalan, and Y. Kushnir (1999), Dominant patterns of climate variability in the Atlantic Ocean during the last 136 years, *J. Clim.*, *12*, 2285–2299.

Tréguier, A. M., et al. (2001), An eddy permitting model of the Atlantic circulation: Evaluating open boundary conditions, *J. Geophys. Res.*, *106*, 22,115–22,129.

Vauclair, F., and Y. du Penhoat (2001), Interannual variability of the upper layer of the Atlantic Ocean from in situ data between 1979 and 1999, *Clim. Dyn.*, *17*, 527–546.

Wang, C. (2002), Atlantic climate variability and its associated atmospheric circulation cells, *J. Clim.*, *15*, 1516–1536.

Weare, B. C. (1977), Emperical orthogonal analysis of Atlantic Ocean surface temperatures, *Q. J. R. Meteorol. Soc.*, *103*, 467–478.

Zebiak, S. E. (1993), Air-Sea interaction in the equatorial Atlantic region, *J. Clim.*, *6*, 1567–1586.

N. Ayoub, P. De Mey, Y. du Penhoat, and S. Illig, LEGOS, UM 5566 (CNES-CNRS-IRD-UPS), 14 av. E. Belin, F-31400 Toulouse, France. (illig@notos.cst.cnes.fr)

F. Bonjean and G. S. E. Lagerloef, ESR, 1910 Fairview Ave East, Suite 102, Seattle, WA 98102, USA.

B. Dewitte, IRD-LEGOS, BPA5, F-98848 Nouméa, New Caledonia.

G. Reverdin, LODYC, Case 100, 4 pl. Jussieu, F-75252 Paris, France.

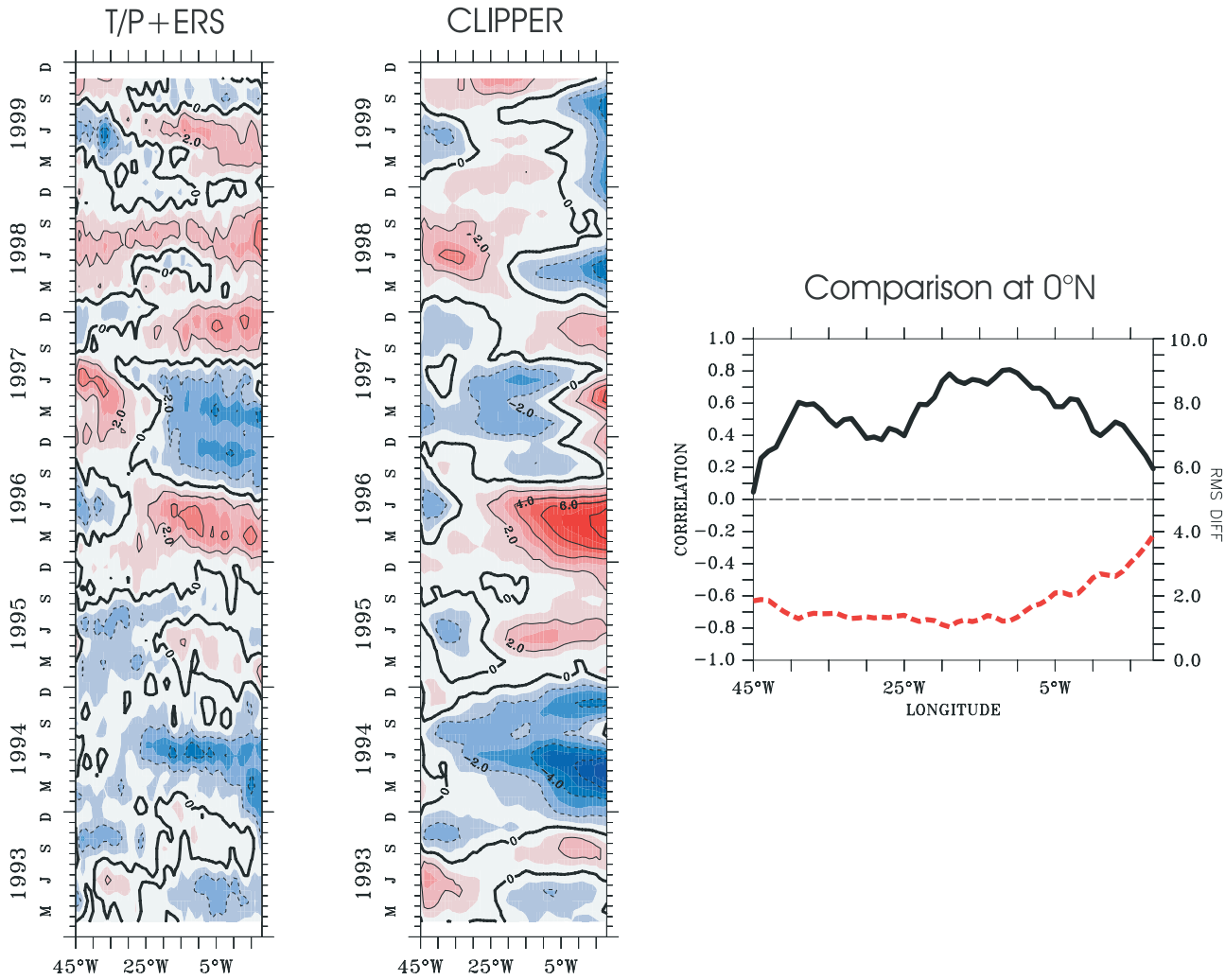

Figure 3. Longitude-time plot of T/P+ERS SLA and CLIPPER SLA along the equator over 1993–1999. Anomalies are relative to the seasonal cycle computed over 1993–1999. Unit is cm. CI is 2 cm. Positive values are red shaded, and negative values are blue shaded. (right) Plots of correlation (black thick line) and RMS difference (red dashed line) between CLIPPER and T/P+ERS for SLA are displayed.